Crystal Engineering as Efficient Medicinal Chemistry Tool for Bioavailability Enhancement in High-Dose Animal PK Studies in Early Pre-Clinical Research

Axel Becker *, Carolina von Essen , Lars Burgdorf , Marc Lecomte , Daniel Bischof

Posted Date: 30 March 2026

doi: 10.20944/preprints202603.2301.v1

Keywords: co-crystal; crystal engineering; supersaturation; in-vivo exposure; crystal structure; surface hydrophilicity

 doi:10.20944/preprints202603.2301.v1

Article

Crystal Engineering as Efficient Medicinal Chemistry Tool for Bioavailability Enhancement in High-Dose Animal PK Studies in Early Pre-Clinical Research

Axel Becker [1,*], Carolina von Essen [1], Lars Burgdorf [2], Marc Lecomte [2] and Daniel Bischof [3]

[1] Merck KGaA, Site Management – Lab Services

[2] Merck Healthcare KGaA, Global Research & Development

[3] Merck Life Science KGaA, Process Solutions

* Correspondence: axel.becker@merckgroup.com

Abstract

Background: A lean crystal engineering study was performed on early pre-clinical POLθ inhibitor MSC178 to enable sufficient exposure for high-dose PK studies. **Methods:** COSMOquick derived excess enthalpies in combination with toxicological assessment of co-formers were used for selection of four co-formers. Experimental crystallization trials were performed in a staged approach from 15 mg-scale over 50 mg upscale to final g-scale upscale of most promising co-crystal form with 2,4-DHBA. **Results:** 2,4-DHBA co-crystal form revealed a more enhanced and sustained supersaturation profile in biorelevant non-sink dissolution test compared to amorphous free base form as well as compared to 3,4-DHBA co-crystal form and 1,2-EDSA salt form. Moreover, 2,4-DHBA co-crystal form was shown to be physically stable in suspension vehicle for PK study. The high physical stability towards physical form conversion in the suspension vehicle as well as the more sustained supersaturation behavior in non-sink dissolution profile could be attributed to intrinsic features of the crystal structure as well as surface hydrophilicity assessment of the co-crystal particles, both suggesting that rather hydrophobic surfaces are present that aid to preferably attract stabilizing surfactants from the dissolution medium (taurocholate) and from the suspension vehicle (polysorbate, methocel), respectively. Successful upscale of the 2,4-DHBA co-crystal form was achieved in small g-scale, revealing mainly isotropic crystal growth in primary particles as well as pronounced tendency for isotropically shaped dendrite-like secondary particles, both being favored by multi-dimensional hydrogen bonding network being present. Resulting favorable powder properties are also deemed highly promising for application in more sophisticated formulation vehicles such as Powder-In-Capsules for higher species animal PK studies. Excellent agreement was shown for extent of in-vitro supersaturation behavior and in-vivo exposure gain in high-dose PK study for the 2,4-DHBA co-crystal form vs amorphous free form. **Conclusion:** Co-crystal strategy can be successfully developed in early pre-clinical industrial research with lean methodologies to optimize sub-optimal phys.-chem. properties of a free base compound to achieve improved and less variable in-vivo exposure between animals in high-dose PK studies.

Keywords: co-crystal; crystal engineering; supersaturation; in-vivo exposure; crystal structure; surface hydrophilicity

1. Introduction

New chemical entity (NCE) drugs were the majority of approved drugs for the last 20 years and remain the backbone of approved drugs also in recent years based on FDA approvals [1]. However, poor aqueous solubility is a recurring and even growing trend in current NCE discovery and development. Alongside with these in-vitro constraints, limitations in oral bioavailability for in-vivo studies are typically observed [2,3]. These challenges are further intensifying for new class of beyond-

 doi:10.20944/preprints202603.2301.v1

rule-of-5 drugs such as PROTACs [4]. Although i.v.-administration of parenteral API solutions may be pursued to achieve highest possible plasma levels, it is generally envisaged early in drug discovery and development to provide orally bioavailable delivery forms also for animal PK studies, as i.v.-administration has even higher demands on compound properties (such as solubility). Typical approaches to overcome the solubility limitations of NCEs to achieve this are targeted in early formulation development, among others crystal engineering, self-emulsifying drug delivery systems (SEDDS), amorphous solid dispersions (ASDs) obtained by spray-dried dispersions (SDD) or hot-melt-extrusion (HME) processes [2,5]. However, all of these tools typically require systematic experimental screening and are typically done in late research or early development stage where larger compound quantities and more extended development timelines are ensured to allow this.

In early MedChem research, in-vivo-profiling of candidates is typically done by vehicle screenings comprising solubility-enhancing excipients such as cyclodextrins, surfactants, or organic co-solvents. However, such rather generic technologies may not suffice for poorly soluble compounds to achieve solution vehicles in desirable concentration, whereas suspension vehicles can lack sufficient exposure for poorly soluble compounds. In such cases, suspension vehicles based on optimized solid-state forms from crystal engineering approaches may be utilized as alternatives [6].

Here we report a lean crystal engineering study to overcome such solubility constraints for novel Polθ polymerase-domain (POLθ) inhibitor MSC178 to provide an orally bio-available tool compound for this class of compounds to study in-vivo exposure. DNA polymerase θ is a central mediator of microhomology-mediated end-joining (MMEJ) and represents a promising synthetic lethal target in tumors with defects in homologous recombination and other DNA damage response (DDR) pathways. Defects in canonical DNA damage response pathways such as non-homologous end-joining (NHEJ), Fanconi anemia (FA), and homologous recombination (HR) can create a strong dependency on Polθ-mediated repair, thereby establishing a synthetic lethal relationship between Polθ and these DDR pathways. Polθ is upregulated in several human malignancies, including breast, ovarian, lung, liver and brain cancers, and elevated Polθ expression correlates with poor prognosis in, for example, lung cancer, soft tissue sarcoma, breast cancer and glioma. [7–10].

POLθ inhibitor MSC178 represents a very weak base, with basic pK_a of 2.6, which can most likely be attributed to the methyl-pyrazole nitrogen. This makes salt formation in principal feasible, however, strong acids are needed. The compound is rather lipophilic, with log P of 3.0. All physicochemical properties are within rule-of-five structural space [11]. Molecular structure of MSC178 is displayed in Figure 1. Corresponding physicochemical properties are summarized in Table 1.

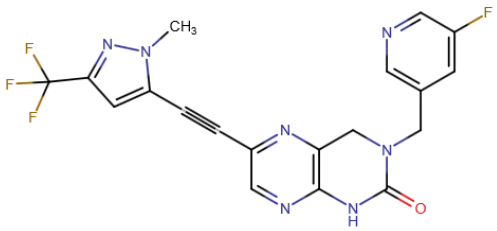

Figure 1. Chemical structure of MSC178.

Table 1. Physicochemical properties of MSC178A (free form).

Parameter	Value
Molecular weight	431.35 g/mol
HBD / HBA	1 / 8
pK_a	2.60[1], 9.80[2]
log P	3.0[3]
log D	3.2[3]

 doi:10.20944/preprints202603.2301.v1

[1] basic pK_a (UV-titration), [2] acidic pK_a (UV-titration), [3] measured (shaked-flask method).

Vehicle screening was performed with amorphous form of MSC178A (free form) in a range of generic solubilizing media, with target to obtain a solution vehicle for p.o. administration in high-dose PK studies with envisaged vehicle solution concentrations of 1 mg/mL and 5 mg/mL, respectively:

- 20% Kolliphor HS 15 in water
- 20% PEG-400 in water
- 20% Glycofurol in water
- 20% Kleptose (HPB) in water and 40% Kleptose (HPB) in water
- 20% Captisol in water
- 2% Tween-80, 12% Kolliphor EL in water
- 10% Kolliphor P 188 in water
- 10% NMP in PEG-300

None of these solubilizing vehicles yielded a visually clear solution even at lower targeted concentration of 1 mg/mL. All vehicles were subsequently diluted 1:1 with blank vehicle to yield solution concentration of 0.5 mg/mL, however, also under these diluted conditions no vehicle yielded a visually clear solution. Consequently, MSC178A (free form, amorphous) is insufficiently soluble (<0.5 mg/mL) for solution vehicles for intended high-dose PK study in a broad range of solubilizing vehicles.

Different formulations options were considered as alternatives to solution vehicles for the planned high-dose PK study, under consideration of required compound needs of MSC178A free form for feasibility assessment, required time needed for lab-based feasibility options, and anticipated probability of success to obtain a formulation with improved exposure in high-dose animal PK studies. Among these options, nanosuspension of free form was ruled out due to high compound need and low probability of success (compound anticipated to be solubility-limited as opposed to dissolution-rate limited according to DCS classification [12]), amorphous solid dispersion was discarded due to prolonged turn-around times, and advanced vehicle screening was not pursued due to expected low probability of success to achieve a solution vehicle with required concentration levels. A lean crystal engineering approach was selected as most viable option to meet low compound requirement for feasibility study, quick turnaround time for feasibility study, and a reasonable expected probability of success to improve exposure based on literature data [6,13]. Identified alternative solid-state forms were aimed for assessment of suspension vehicle stability.

Whereas conceptional studies on co-crystal formation for improving solubility and in-vivo exposure are widely published mainly on model compounds [6,14,15], to the best of our knowledge, this is one of rare publications to show that a miniaturized and lean crystal engineering approach is a powerful technology to provide efficient design of fit-for-purpose solid-state forms with improved in-vivo exposure for in-vivo profiling of drug candidates in early pre-clinical research from pharmaceutical industry.

This article further outlines specific benefits of co-crystal forms vs salt forms of same API structure to achieve enhanced in-vitro solubility and supersaturation in combination with improved physicochemical aspects such as physical stability (as also highlighted by Cavanagh et al. [16]).

The study further provides valuable insights on why some crystal engineered forms are capable to achieve in-vitro and in-vivo supersaturation, whereas other forms from crystal engineering fail to do so.

Finally, this article illustrates how PAT-supported lab-scale upscale can be efficiently utilized in early pre-clinical research for controlled manufacturing of g-scale quantities for comprehensive PK studies.

 doi:10.20944/preprints202603.2301.v1

2. Results

All data and results reported here are based on POLθ inhibitor MSC178 as exemplary drug candidate in early research phase with a challenging physicochemical properties profile, as initially outlined.

2.1. Lean Crystal Engineering of MSC178A

2.1.1. In-Silico Assessment for Suitable Co-Formers for Salts and Co-Crystals

Selection of most promising co-formers for co-crystal formation was based on excess enthalpy calculation in hetero dimers (co-former vs MSC178) via COSMO-RS theory performed in COSMOQUICK software [17]. To accomplish a lean screening design, only highly-ranked selected co-formers which were pre-aligned with Merck Healthcare internal toxicology department were considered for experimental studies:

- Hydrochloric acid is ubiquitously present as endogenous agent.
- 1,2-Ethanedisulfonic acid is part of pre-aligned Merck healthcare internal acid list for salt formation, and can be found as counter-ion in FDA Orange Book analysis [18]
- 2,4-Dihydroxybenzoic acid is a degradation product of cyanidin glycosides from tart cherries in cell cultures [19], and also a metabolite found in human plasma after cranberry juice consumption [20].
- 3,4-Dihydroxybenzoic acid is major metabolite of antioxidant polyphenols found in green tea [21].

Results of excess enthalpy calculations for selected co-formers are shown in Table 2. All four co-formers, regardless of salt formation or co-crystal formation scope, exhibit reasonably negative calculated excess enthalpies in dimeric interaction with MSC178. Hence, crystallization of a tailored mixed crystal form with these co-formers was deemed promising, and all four co-formers were selected for first co-crystallization trials.

Table 2. Results of in-silico prediction (COSMOQUICK) of toxicology-accepted co-formers.

Co-former	Excess enthalpy H_{ex}	pK_a (DpKa vs MSC178) [1]
Hydrochloric acid (HCl)	-3.3 kcal/mol	-5.9 (8.5) [2]
3,4-Dihydroxybenzoic acid (3,4-DHBA)	-3.5 kcal/mol	4.48 (1.88) [3]
2,4-Dihydroxybenzoic acid (2,4-DHBA)	-4.5 kcal/mol	3.11 (0.51) [3]
1,2 Ethanedisulfonic acid (1,2-EDSA)	-5.5 kcal/mol	-1.46 (4.06) [2] -2.06 (4.66) [2]

[1] All pKa values from https://en.wikipedia.org/ (accessed 13.01.2026), [2] salt formation aimed for based on ΔpKa co-former vs MSC178; [3] co-crystal formation aimed for based on ΔpKa co-former vs MSC178.

Looking at rank order of excess enthalpies, strongest dimeric interaction is suggested between MSC178A and 1,2-EDSA. As sulfonic acids bear highly polarized functional groups, this appears plausible as COSMO theory calculated interaction strength based on electrostatic surface charge profiles (σ-profiles) and interaction of most polarized surface charge spots [22]. For same reason, a slightly stronger interaction between 2,4-DHBA vs 3,4-DHBA is reasonable, as the hydroxy group in alpha position to carboxylic acid function in 2,4-DHBA allows an additional intramolecular hydrogen bond, giving rise to an overall more polarized functional group (also seen in more acidic pK_a in 2,4-DHBA).

 doi:10.20944/preprints202603.2301.v1

2.1.2. Miniaturized Salt- and Co-Crystal Formation Trials

In order to apply a cooling crystallization process for co-crystal formation, a condensed solubility assessment was made for MSC178A (free form, amorphous) and both dihydroxybenzoic acid co-formers intended for co-crystal formation. Solubility was assessed in three organic process solvents (acetonitrile, 1,4-dioxane, ethyl acetate) to with medium polarity to allow sufficient solubilization of lipophilic API compound as well as of more hydrophilic co-formers (hence excluding alcohols as too polar solvents and aromatic solvents as too non-polar solvents). Results of solubility assessment are shown in Table 3.

Table 3. Solubility assessment (50 °C) in selected organic process solvents.

Solvent (rel. polarity [1])	Solubility MSC178A	Solubility 2,4-DHBA	Solubility 3,4-DHBA
acetonitrile (0.46)	~9 mg/mL	~29 mg/mL	~6 mg/mL
ethyl acetate (0.228)	~11 mg/mL	~55 mg/mL	>30 mg/mL
1,4-dioxane (0.164)	>46 mg/mL	>240 mg/mL	~85 mg/mL

[1] Relative solvent polarities: hexane = 0.009, water = 1 [23].

Based on solubility data, acetonitrile and ethyl acetate were selected as crystallization solvents, whereas 1,4-Dioxane was deemed as too good solvent for MSC178A as well as for the co-formers. Significant higher solubility of MSC178A in 1,4-dioxane compared to acetonitrile and ethyl acetate can be explained by lowest polarity of dioxane among the three solvents. The fact that 1,4-dioxane also exhibits best solubilization for both co-formers may be attributed to hydrogen bonding potential of 1,4-dioxane to carboxyl acid groups [24]. Higher solubility of both dihydroxybenzoic acid co-formers in ethyl acetate compared to acetonitrile can be attributed to more hydrogen bonding options being possible between co-formers and ethyl acetate.

A first cooling crystallization panel was run at 15 mg scale (quantity of MSC178A), with results summarized in Table 4. New crystalline forms were obtained from all initial co-crystallization experiments. Samples from acetonitrile exhibited more favorable properties for HCl, 2,4-DHBA, and 3,4-DHBA, as crystallizations from ethyl acetate for these co-crystals yielded increased incorporation of ethyl acetate in crystal lattice or formation of acetic acid in case of HCl. Also, strongly over-stoichiometric ratios of co-former were retrieved in ethyl acetate trials with 2,4-DHBA and with 3,4-DHBA. Therefore, acetonitrile was selected as preferred solvent for a small upscale to 50 mg scale for these 3 co-crystals. Based on superior crystallinity in obtained co-crystal form, co-crystallization with 1,2-EDSA was preferred from ethyl acetate, which was consequently selected as solvent for small upscale of 1,2-EDSA co-crystal/salt.

Table 4. Summary of co-crystallizations (cooling crystallizations, 15 mg scale).

Co-former	Solvent	Analytical data solid-state residue		
		Crystallinity[1]	Stoichiometry[2]	Residual solvents[3]
HCl	acetonitrile	Crystalline, form Cl-1	0.9 eq. chloride	MeCN n.d.
	ethyl acetate	Crystalline, form Cl-2	0.9 eq. chloride	EtOAc n.d., acetic acid 1.0 eq.
1,2-EDSA	acetonitrile	Poorly crystalline, form Ed-1	0.7 eq. 1,2-EDSA	MeCN n.d.
	ethyl acetate	Crystalline, form Ed-2	0.7 eq. 1,2-EDSA	EtOAc 0.02 eq.
2,4-DHBA	acetonitrile	Crystalline, form 24-1	1.1 eq. 2,4-DHBA	MeCN n.d.
	ethyl acetate	Crystalline, form 24-2 [4]	3.6 eq. 2,4-DHBA	EtOAc 0.4 eq.

 doi:10.20944/preprints202603.2301.v1

3,4-DHBA	acetonitrile	Crystalline, form 34-1	1.3 eq. 3,4-DHBA	MeCN n.d.
	ethyl acetate	Crystalline, form 34-2 [4]	2.1 eq. 3,4-DHBA	EtOAc 1.0 eq.

[1] Powder X-Ray Diffraction, [2] ^{1}H-NMR or IC (chloride), [3] ^{1}H-NMR, [4] hints for signals of excess free co-former.

To account for slight deviations in retrieved stoichiometric ratios compared to expected ratios in case of 1,2-EDA co-crystal (0.7 eq. EDSA retrieved) and in case of 3,4-DHBA co-crystal (1.3 eq. DHBA retrieved), the 50 mg upscale trials were slightly amended regarding co-former quantities to target a mono-co-crystal form for 3,4-DHBA and both a hemi- and a mono-salt form for 1,2-EDSA, respectively (see section 4 for details). Results from cooling crystallization upscales at 50 mg scale (quantity of MSC178A) are summarized in Table 5. 50 mg upscale experiments yielded highly crystalline co-crystal / salt forms with reasonable stoichiometric ratios (with max. deviation of 0.1-0-2 eq. of co-former equivalents) and no hints for excess free co-former being crystallized as phase mixture. For 1,2-EDSA salts, both a mono -salt (form Ed-2) and a hemi-salt (form Ed-3) could be obtained by adjusting the quantities of sulfonic acid in the reaction. HCl salt form, 1,2-EDSA mono salt form as well as 2,4-DHBA co-crystal and 3,4-DHBA co-crystal forms were successfully reproduced from 10 mg scale. All forms apart from HCl salt form Cl-1 exhibited very low residual solvent level. HCl salt form Cl-1 exhibited slightly increased residual acetonitrile level, however, still under-stoichiometric compared to expected solvent levels for a solvate form. This is probably due to some strong solvent entrapment between particles. All 50 mg samples were selected for further profiling.

Table 5. Summary of optimized co-crystallizations (cooling crystallizations, 50 mg scale).

Co-former	Solvent / target stoichiometry	Analytical data solid-state residue		
		Crystallinity[1]	Stoichiometry[2]	Residual solvents[3]
HCl	acetonitrile / 1:1	Crystalline, form Cl-1	1.1 eq. chloride	MeCN 0.25 eq.
1,2-EDSA	ethyl acetate / 1:1	Crystalline, form Ed-2	1.2 eq. 1,2-EDSA	EtOAc 0.007 eq.
	ethyl acetate / 0.5:1	Crystalline, form Ed-3	0.6 eq. 1,2-EDSA	EtOAc 0.04 eq.
2,4-DHBA	acetonitrile / 1:1	Crystalline, form 24-1	1.2 eq. 2,4-DHBA	MeCN n.d.
3,4-DHBA	acetonitrile / 1:1	Crystalline, form 34-1	1.0 eq. 3,4-DHBA	MeCN n.d.

[1] Powder X-Ray Diffraction, [2] ^{1}H-NMR or IC (chloride), [3] ^{1}H-NMR.

2.2. Solid-State Characterization Data of MSC178 Forms

For selected solid-state forms [1,2-EDSA hemi-salt form Ed-3, 2,4-DHBA co-crystal form 24-1, 3,4-DHBA co-crystal form 34-1] solid-state IR-spectra were recorded in comparison with free base amorphous form, however, no clear conclusions regarding salt form (protonation of API scaffold) vs co-crystal (no protonation) can be deduced from spectra. Based on pK_a values of API and involved acids, salt formation can be assumed as solid-state form in case of HCl and 1,2-EDSA, and co-crystal formation can be assumed as solid-state form in case of 2,4-DHBA and 3,4-DHBA, respectively, in line with FDA guidance for differentiation of salt vs co-crystal forms [25]. In case of 2,4-DHBA form 24-1 and 3,4-DHBA form 34-1, this is also confirmed by Single-Crystal X-Ray Diffractometry and electron diffraction data as shown below.

PXRD patterns of 50 mg scale samples, as outlined in Table 5, are shown in Figure 2. All co-crystal / salt forms can unequivocally be differentiated and identified by their characteristic PXRD profiles. No hints for presence of excess free acid co-formers are observed in case of forms Ed-2, Ed-3, 24-1, and 34-1, respectively. Absence of pronounced underlying broad background halos confirms that no significant amorphous fractions are present in any form. Signal intensities and signal/noise ratio in 1,2-EDSA hemi-salt form Ed-3 is lower than in other forms due to smaller sample quantity in the X-Ray preparation. Although all forms can be deemed as highly crystalline forms based on multitude of sharp signals being observed, slightly broader line width of PXRD signals suggest that 1,2-EDSA hemi-salt form Ed-3 and 3,4- DHBA-co-crystal form 34-1 may exhibit slightly reduced degree of crystallinity.

 doi:10.20944/preprints202603.2301.v1

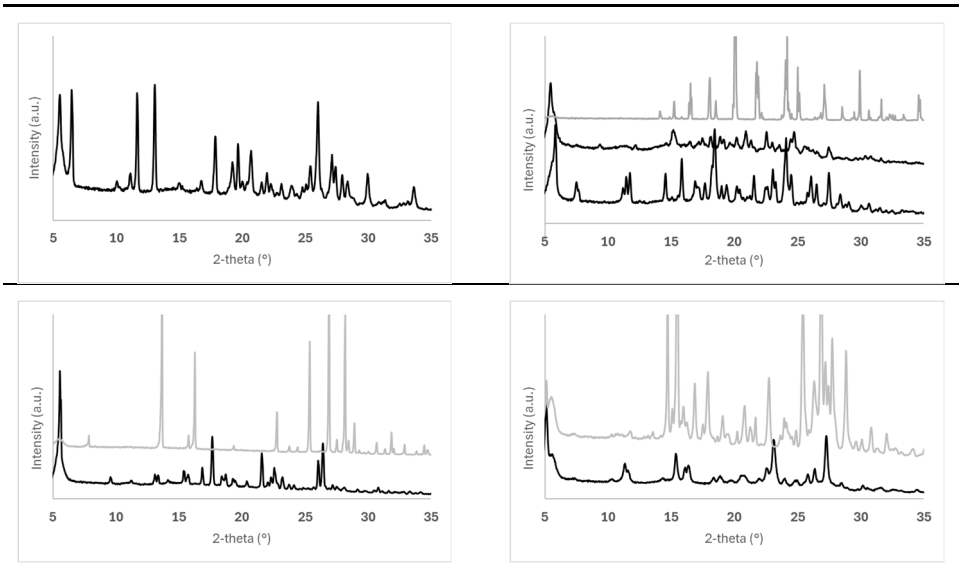

Figure 2. PXRD patterns of co-crystal / salt forms of MSC178. top left: HCl salt form Cl-1. top right: 1,2-EDSA salt forms Ed-2 (bottom) & Ed-3 (middle) vs 1,2-EDSA co-former (top, grey). bottom left: 2,4-DHBA co-crystal form 24-1 (bottom) vs 2,4-DHBA co-former (top, grey). bottom right: 3,4-DHBA co-crystal form 34-1 (bottom) vs 3,4-DHBA co-former (top, grey).

DSC heating scans of 1,2-EDSA hemi-salt form Ed-3, 2,4-DHBA co-crystal form 24-1, and 3,4-DHBA co-crystal form 34-1 are shown in Figure 3. 2,4-DHBA co-crystal form 24-1 exhibits a melting point onset of approx. 203 °C, whereas 3,4-DHBA co-crystal form 34-1 exhibits an overlapped melting peak with initial onset at approx. 178 °C and extrapolated 2nd onset of overlapped main peak at approx. 188 °C, respectively. The broader and overlapping melting peak in 3,4-DHBA co-crystal form can be linked to the slightly decreased degree in crystallinity as deduced from PXRD line widths. Overall, significantly higher melting point in 2,4-DHBA co-crystal may indicate a stronger crystal lattice interaction compared to 3,4-DHBA co-crystal. In contrast to both co-crystal forms, the 1,2-EDSA hemi-salt for Ed-3 exhibits no clear melting peak, but rather an exothermic peak at approx. 218 °C. This can be attributed to thermal decomposition upon heating, and hence it can be concluded that the hemi-edisylate salt form exhibits a virtual melting peak higher than 218 °C. The highest thermal stability in this solid-state form, despite also hints for slightly reduced crystallinity as suggested from PXRD line widths, can be explained by significantly stronger lattice interactions due to ionic interactions in the salt form compared to hydrogen-binding interactions in co-crystal forms.

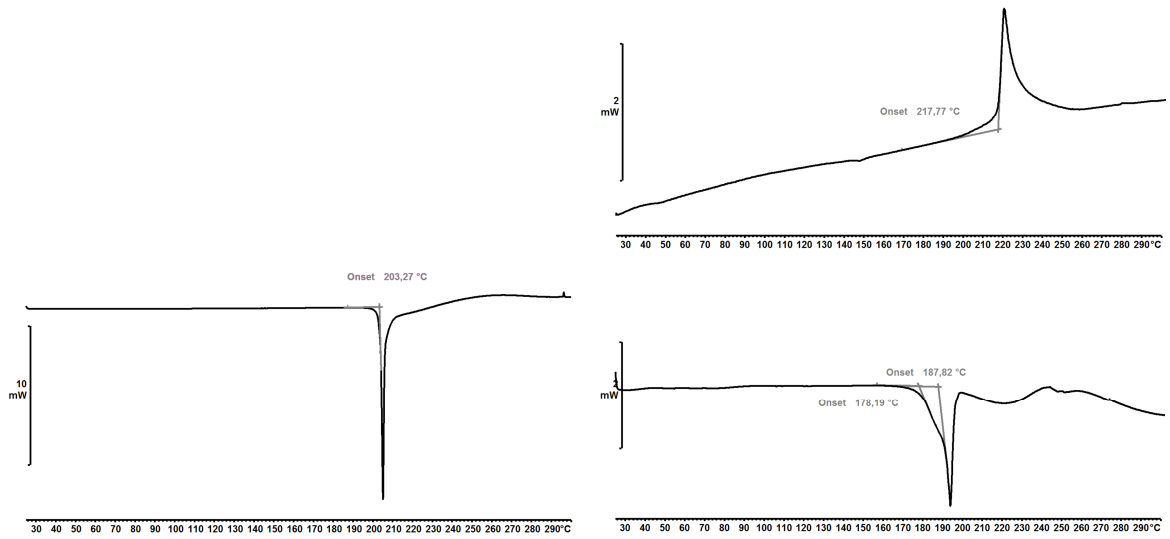

 doi:10.20944/preprints202603.2301.v1

Figure 3. DSC heating traces (exo upwards) of co-crystal / salt forms of MSC178. top right: 1,2-EDSA hemi-salt form Ed-3. bottom left: 2,4-DHBA co-crystal form 24-1. bottom right: 3,4-DHBA co-crystal form 34-1.

For further in-depth characterization of both obtained co-crystal hits, 2,4-DHBA co-crystal form 24-1 and 3,4-DHBA co-crystal form 34-1 were profiled by temperature-modulated DSC (mDSC) for determination of heat capacities Cp as a measure for solid-state mobility of molecules in the crystal lattice. Resulting heat capacity profiles as a function of temperature are shown in Figure 4. It can be seen that 2,4-DHBA co-crystal form 24-1 exhibits lower heat capacity in the investigated temperature range 25-65 °C (0.97-1.07 J/g*K) compared to 3,4-DHBA co-crystal form 34-1 (1.17-1.24 J/g*K), however, these differences are at best borderline significant based on observed scattering of data derived from standard deviations (0.11-0.14 J/g*K) within multiple determinations per form. Nevertheless, as a trend, form 24-1 appears to exhibit lower heat capacity and consequently also lower solid-state related molecular mobility. This suggests a stronger overall coordination of molecules in the crystal lattice of 2,4-DHBA co-crystal form 24-1 compared to those in 3,4-DHBA co-crystal form 34-1. Moreover, form 34-1 also appears to exhibit a very slightly steeper slope in heat capacity changes upon heating, suggesting a slightly stronger solid-state entropy contribution [26]. The heat capacity data also fit well with the observed higher melting point in form 24-1.

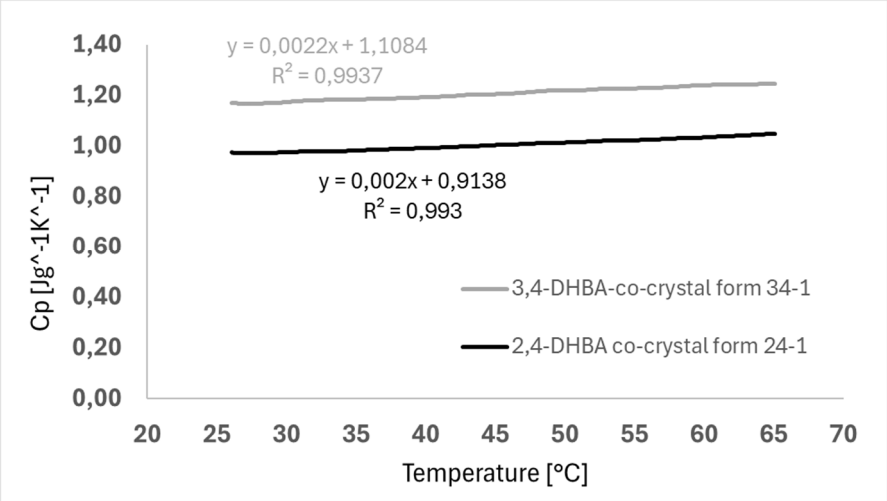

Figure 4. Heat capacity (Cp) vs temperature profiles of 2,4-DHBA co-crystal form 24-1 and 3,4-DHBA co-crystal form 34-1 of MSC178. (mean from 2 samples of each co-crystal form, each measured with n=2; overall mean standard deviation per form: 0.11-0.14 J/g*K).

Water vapor sorption isotherms were acquired at 25 °C for 1,2-EDSA hemi-salt form Ed-3, 2,4-DHBA co-crystal form 24-1, and 3,4-DHBA co-crystal form 34-1 to assess hygroscopicity behavior compared to free base amorphous form. Respective data are shown in Figure 5. Amorphous form of free base exhibits pronounced water uptake throughout entire rh range, and a strong and broad hysteresis upon desorption. This can be attributed to strong contributions of bulk absorption effects into the amorphous matrix. 2,4-DHBA co-crystal form 24-1 exhibits a very flat and fully reversible sorption profile, with maximum water uptake below 0.5% (m/m), being characteristic for solely surface-attached water uptake due to physisorption processes. In contrast to this, 3,4-DHBA co-crystal form 34-1 exhibits a more pronounced water uptake profile, however, still reversible in nature. The pronounced but reversible uptake levels in combination with characteristic strong water uptake step at low rh levels may be indicative for a channel-hydrate sorption behavior. 1,2-EDSA hemi-salt Ed-3 exhibits by far the strongest water uptake at elevated rh-levels >70% rh. Sorption steps are not reaching equilibrium stage, being indicative for deliquescence processes taking place. Although no indication for a hydrate formation step is seen in lower rh-range 0-60% rh, the hemi-salt form exhibits also pronouncedly higher uptake sorption levels in this humidity range compared to 2,4-DHBA co-

 doi:10.20944/preprints202603.2301.v1

crystal form 24-1. This may be explained by higher attraction of water vapor to particle and crystal surfaces due to ionic interactions in the salt crystal lattice, which can trigger water attraction in coordination to ionic centers (e.g as ion associated hydrates) [27].

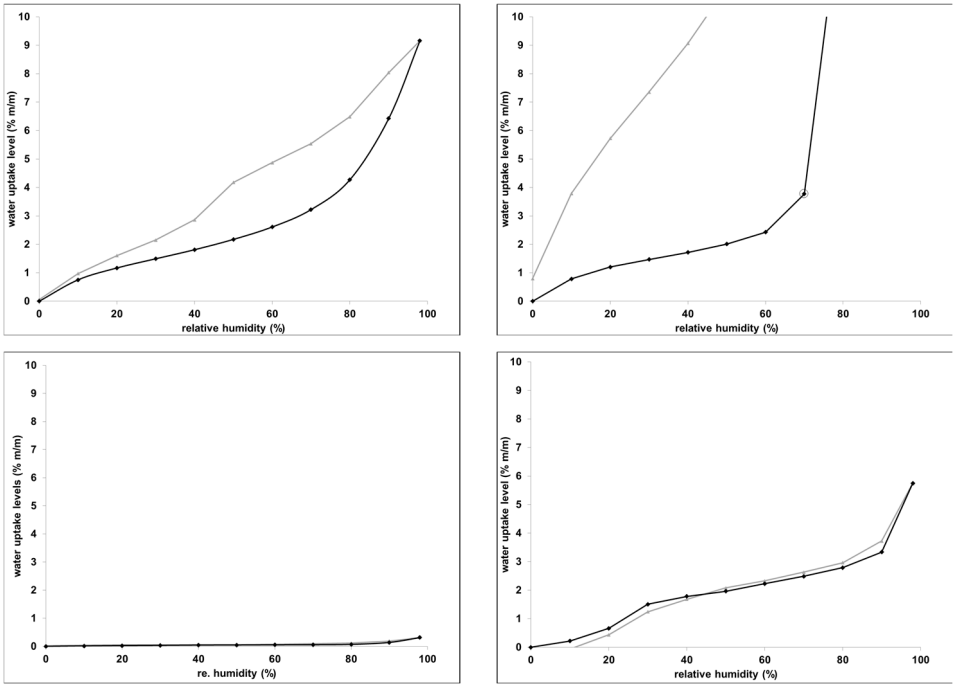

Figure 5. Water vapor sorption isotherms (25 °C) [1] of co-crystal / salt forms of MSC178. (black diamonds: adsorption segment 0-98% rh, grey triangles: desorption segment 98-0% rh). top left: free base MSC178A amorphous form (for comparison). top right: 1,2-EDSA salt form Ed-3. bottom left: 2,4-DHBA co-crystal form 24-1. bottom right: 3,4-DHBA co-crystal form 34-1. [1] y-scale normalized to 0-10% (m/m) for illustration purposes – higher sorption levels in 1,2-EDSA form Ed-3 at elevated rh levels and negative sorption levels in 3,4-DHBA form 34-1 at low rh levels upon desorption are not displayed.

To derive more quantitative description of hydrophilic vs hydrophobic surface domains being present on crystal faces of 2,4-DHBA-co-crystal form 24-1, 3,4-DHBA-co-crystal form 34-1, and 1,2-EDSA salt form Ed-3, water vapor sorption profiles as well as n-octane organic vapor sorption data were acquired in higher partial pressure resolution of 5-50% partial pressure percentage sorption levels. As the BET sorption model is not valid for water vapor sorption data (due to gas-gas interactions and cluster adsorption), a water monolayer equivalent coverage was determined based on sorption equivalent of strongest interaction according to Excess Surface Work (ESW) sorption model [28] and converted into water-specific surface area equivalent as a quantitative measure for surface hydrophilic domains. For assessment of hydrophobic surface area in same samples, BET sorption model was applied on n-octane gravimetric vapor sorption [29]. Water vapor sorption data based on ESW model and n-octane sorption data based on BET model for 1,2-EDA salt, 2,4-DHBA co-crystal, and 3,4-DHBA co-crystal in comparison with free base amorphous form are shown in Figure 6 and resulting surface area equivalents are summarized in Table 6. The sorption data reveal that 2,4-DHBA cocrystal exhibits a pronouncedly lower hydrophilic surface domain compared to 1,2-EDSA salt, both in total water-specific surface area equivalent as well as in relative surface hydrophilic ratio. 3,4-DHBA co-crystal form 34-1 exhibits pronouncedly highest total water-specific surface area equivalent compared to both forms, however, when looking at surface hydrophilic ratio, form 34-1 lies somewhat in-between the apparently more hydrophobic 2,4-DHBA-co-crystal form 24-1 and the apparently more hydrophilic 1,2-NDSA salt form Ed-3. The highest total water-specific surface area equivalent may be explained by the assumed channel structure in this form, as indicated by the full adsorption/desorption isotherms in water vapor sorption and the crystal structure. The surface hydrophilic ratios indicate that co-crystal forms have overall less hydrophilic surface

 doi:10.20944/preprints202603.2301.v1

chemistry in their crystal planes compared to the salt form, however, pronounced differences in surface hydrophilicity can still be observed among different co-crystal structures. It is interesting to note that the free base amorphous form, which was investigated for comparison, exhibits an apparently higher surface hydrophilic ratio than 2,4-DHBA co-crystal form 24-1 despite not bearing any polar co-former / counter-ion in the solid-state structure. Here, potential contributions from bulk absorption effects (as opposed to mere surface adsorption effects) may play a role as well. As 1,2-EDSA salt and 3,4-DHBA co-crystal reveal higher surface hydrophilic ratios compared to amorphous free base (as one would expect for such mixed crystal systems with polar co-formers), this still shows the extraordinarily low surface hydrophilicity in the 2,4-DHBA co-crystal structure.

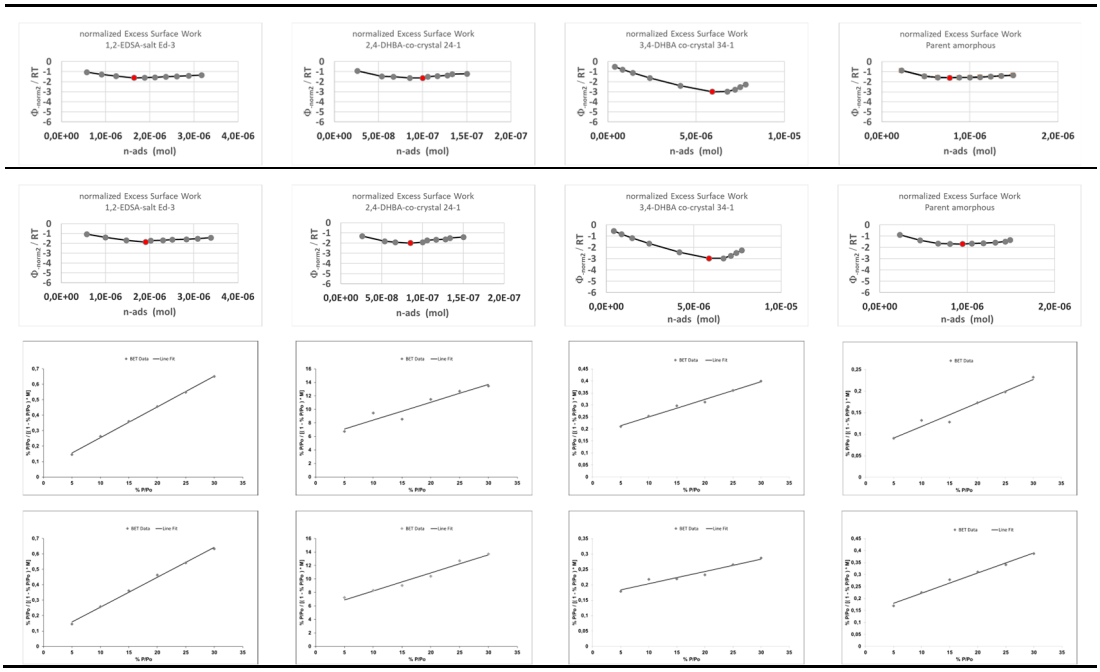

Figure 6. Water vapor and n-octane sorption data of MSC178 1,2-EDSA salt, 2,4-DHBA co-crystal, and 3,4-DHBA salt for assessment of surface area domains (partial pressure steps of 5% from 0-50% partial pressure). Top two rows: water vapor sorption data, ESW model, 2 runs (ESW minimum point shown in red); bottom two rows: n-octane sorption data, BET-model, 2 runs. From left to right: 1,2-EDSA salt form Ed-3, 2,4-DHBA co-crystal form 24-1, 3,4-DHBA co-crystal form 34-1, amorphous free base.

Table 6. Summary of surface area data derived for MSC178 1,2-EDSA salt, 2,4-DHBA co-crystal, 3,4-DHBA salt vs amorphous free base (for comparison) (mean from n=2 determinations per form).

Solid-state form	Water vapor sorption ESW model	n-octane sorption BET model	Surface hydrophilic ratio [1]
1,2-EDSA salt form Ed-3	water-specific surface area equivalent: 2.83 m²/g	n-octane specific surface area: 8.38 m²/g	0.34
2,4-DHBA co-crystal form 24-1	water-specific surface area equivalent: 0.06 m²/g	n-octane specific surface area: 0.52 m²/g	0.11
3,4-DHBA co-crystal form 34-1	water-specific surface area equivalent: 5.28 m²/g	n-octane specific surface area: 24.38 m²/g	0.22
free base amorphous form	water-specific surface area equivalent: 4.51 m²/g	n-octane specific surface area: 22.60 m²/g	0.20

[1] water-specific surface area equivalent (ESW-model) / n-octane surface area (BET-model).

Overall, the sorption data substantiate differences in surface chemistry between salt vs co-crystal forms in a more quantitative and illustrative manner.

 doi:10.20944/preprints202603.2301.v1

Crystal structures could successfully be solved for 2,4-DHBA co-crystal form 24-1, and 3,4-DHBA co-crystal form 34-1. Residual electron density clearly revealed the correct hydrogen positions confirming the presence of a co-crystal form. Hydrogen bonding network of 2,4-DHBA co-crystal form 24-1 is shown in Figure 7. The parent molecule forms homosynthons through interactions between two 3,4-dihydro-1H-pteridin-2-one moieties (N3-H…N4). Additionally, two 2,4-dihydroxybenzoic acid (2,4-DHBA) molecules interact via carboxylic acid–carboxylic acid interactions. These homosynthons are interconnected by hydrogen bonds between the para-hydroxyl group of 2,4-DHBA and the nitrogen N1 of pyridine, resulting in one-dimensional chains. The ortho-hydroxyl group on 2,4-DHBA forms an intramolecular hydrogen bonds (OH hydroxyl…OC carboxyl), which aligns with one of Etter's principles: "*6-membered-ring intramolecular hydrogen bonds preferentially form over intermolecular hydrogen bonds*." [30]. Furthermore, the crystal structure is stabilized by aromatic interactions between pyrazine and benzene, as well as between adjacent pyrazole moieties. Hydrogen bonding network of 3,4-DHBA co-crystal form 34-1 is shown in Figure 8. The structure contains channels surrounded by the hydroxyl groups of the 3,4-DHBA along the crystallographic a-axis. This confirms the observations made in the DVS as well as water vapor sorption profiles. The hydrogen bonding motifs are remarkably similar compared to form 24-1. Homo-synthons between the two parent molecules as well as the co-former are observed with the parent being connected through amide-amide (N3-H…O1) interactions. The co-former is connected by hydrogen bonds between the meta-hydroxyl group and the pyridine nitrogen. The para-hydroxyl group of the acid does not show any hydrogen bonding but is very close to the void channels, presumably interacting with water molecules. The packing arrangements of the crystal structures are shown in Figure 9. It can be seen that in form 24-1, the co-former homosynthons are enclosed by API molecules while in 34-1 adjacent chains of API and co-crystal molecules with voids running in parallel are formed.

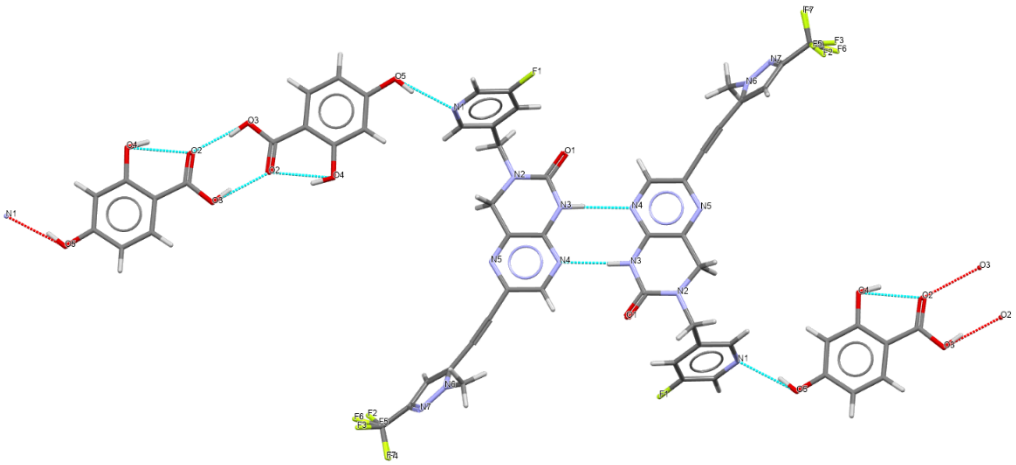

Figure 7. Hydrogen-bond network from crystal structure solution of 2,4-DHBA co-crystal form 24-1.

 doi:10.20944/preprints202603.2301.v1

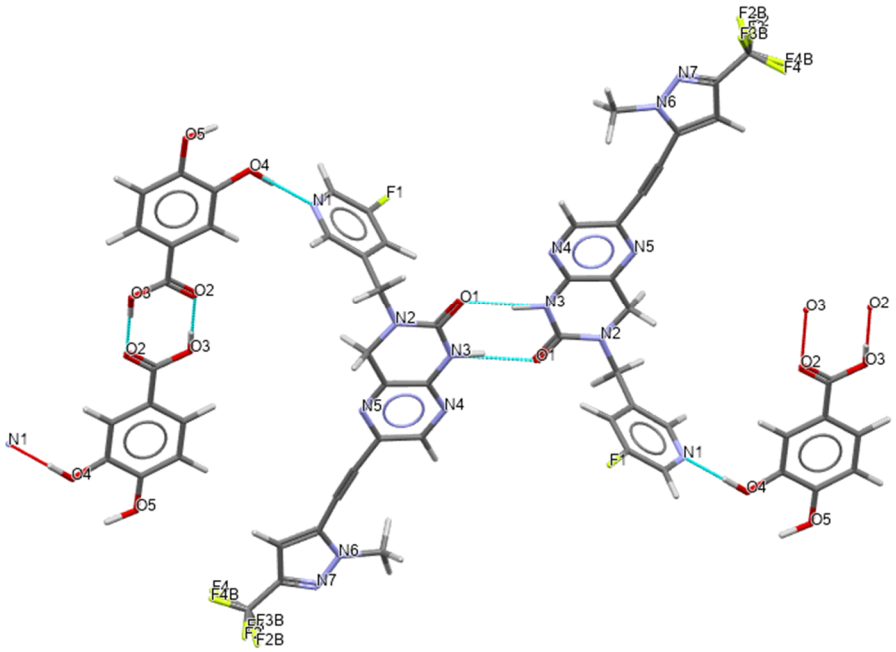

Figure 8. Hydrogen-bond network from crystal structure solution of 3,4-DHBA co-crystal form 34-1.

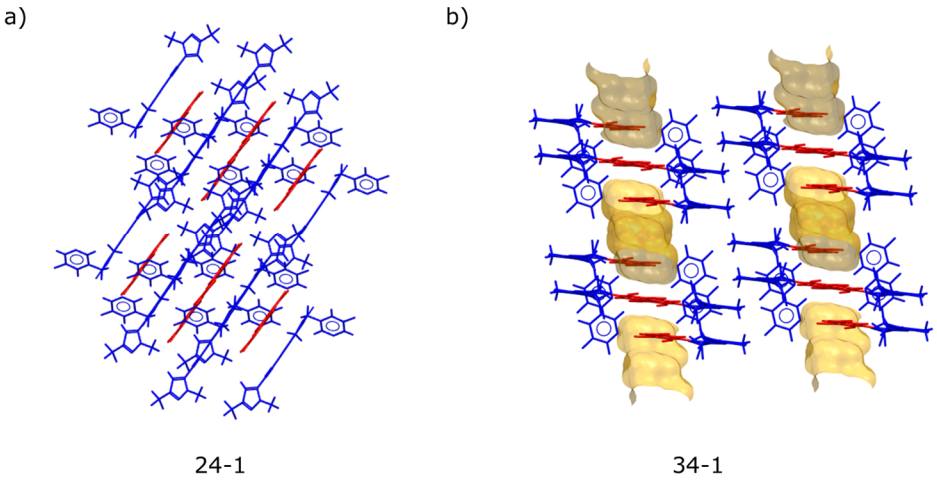

Figure 9. Packing arrangements and voids in the crystal structures of a) 2,4-DHBA and b) 3,4-DHBA co-crystals. API molecules are represented in blue, while co-former molecules are depicted in red.

Crystal morphologies of the 2,4-DHBA co-crystal and 3,4-DHBA co-crystal were computed using the Bravais–Friedel–Donnay–Harker (BFDH) method [31]. included in the latest release of the visualization software package [32]. It calculates approximate crystal morphology based on crystallographic geometrical consideration, including the unit cell shape and symmetry operator information. The BFDH assessment shows that hydrophobic pyrazole and fluoropyridines are exposed at the main faces of the crystal of form 24-1, whereas the dominating faces of form 34-1 exhibit the polar hydroxyl groups.

 doi:10.20944/preprints202603.2301.v1

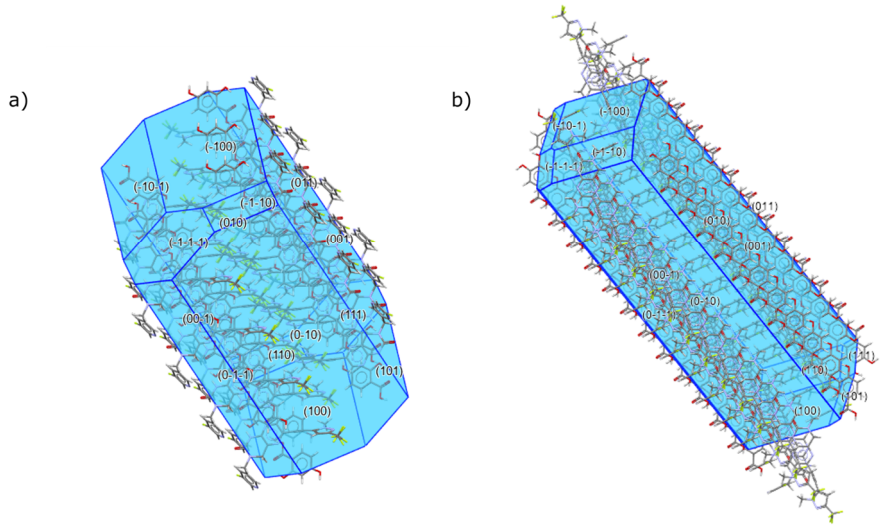

Figure 10. BFDH predicted morphology of the a) 2,4-DHBA and b) 3,4-DHBA co-crystal.

2.3. In-Vitro Biopharmaceutical Assessment of Crystal Forms

2.3.1. Non-Sink Miniaturized Dissolution Assessment

Successfully obtained co-crystal and salt forms from 50 mg upscale were profiles for potential improvement in dissolution behavior compared to amorphous free form under non-sink conditions in biorelevant intestinal medium (FaSSIF) to mimick in-vivo-conditions [33].

Resulting non-sink dissolution profiles are displayed in Figure 11. It can be seen that 2,4-DHBA co-crystal form 24-1 as well as 1,2-NDSA hemi-salt form Ed-3 exhibit enhanced levels of dissolved API upon non-sink dissolution compared to amorphous free form (c-max [30 min] level increased by factor 2 [hemi-salt form Ed-3] and factor 2.5 [co-crystal form 24-1], respectively). Moreover, this superstauration effect appears to be stable up to 30 min at least, whereas at 60 min and at 120 min a very slight decrease in dissolution levels are observed for both crystalline forms, which may be indicative for a starting precipitation of a less soluble parent form. The fact that these two crystalline forms exhibit higher disolution levels compared to amorphous free base suggests that the solubility constraints of the free form is not driven by lattice energy effects (no “brick-stone” compound), but rather by limitations in solubilization due to insufficient hydration energy (“grease-ball” compound), also supported by high log P value as strongly contributing factor for poor solubility [34]. Enhanced dissolution behaviour of the edisylate salt form is likely driven by enhanced solubility of protonated compound in the diffusion boundary layer [35]. However, corresponding mono-edisylate salt form Ed-2 does not show any dissolution improvement, which may be impaired by the apparently higher crystallinity in the mono-edisylate salt compared to hemi edisylate salt form. It is also interesting to note that no enhanced dissolution levels are observed for alternative co-crystal form 34-1 with 3,4-DHBA as co-former, despite the apparent hint for slightly reduced crystallinity in this form compared to 2,4-DHBA co-crystal form 24-1. HCl salt form Cl-1 exhibits the lowest dissolution level among all forms, which can be explained by solubility decrease due to common-ion effect of chloride ions from FaSSIF [35]. Although HCl salt form appears to be the least soluble and hence most stable form in such medium with excess levels of dissolved chloride ions, none of the other forms shows a pronounced precipitation effect down to the lower dissolution levels of the HCl salt form even up to 120 min in the dissolution medium. This is understood to be inhibited due to potential energy barriers for nucleation of the HCl salt form.

 doi:10.20944/preprints202603.2301.v1

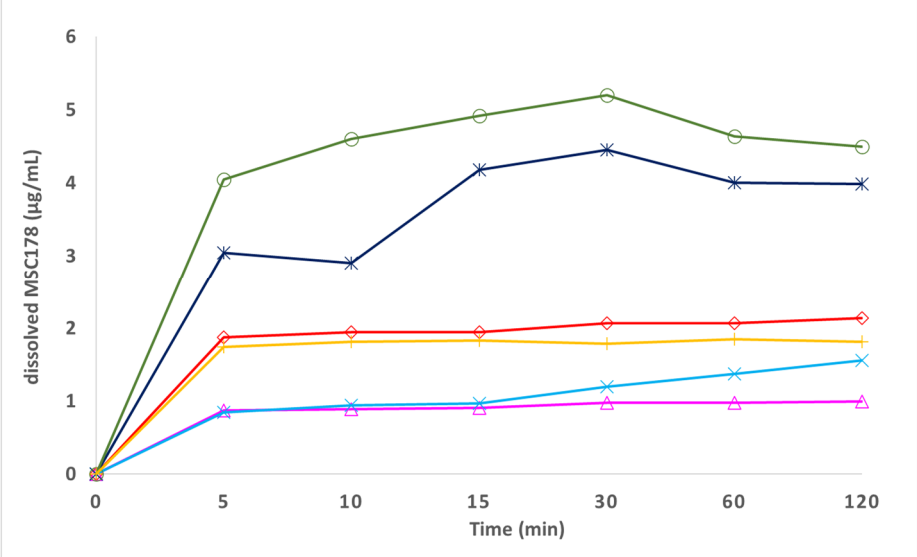

Figure 11. Non-sink dissolution profiles of solid-state forms of MSC178 in FaSSIF (pH 6.5), 37 °C (mean from n=2). green circles: 2,4-DHBA co-crystal form 24-1. dark blue stars: 1,2-EDSA hemi-salt form Ed-3. red diamonds: free base MSC178A amorphous form. orange dashes : 3,4-DHBA co-crystal form 34-1. light blue crosses: 1,2-EDSA mono-salt form Ed-2. magenta triangles: HCl-salt Cl-1.

2.3.2. Vehicle Stability Assessment of Lead Forms

Based on observed supersaturation levels in-vitro non-sink disolution assay, 1,2-EDSA hemi-salt form Ed-3 and 2,4-DHBA co-crystal form 24-1 were selected for in-vivo high-dose PK studies for assessment of in-vivo exposure from p.o. administration. A methocel/tween suspension (0.5% methocel, 0.25% tween-20 in water) was selected as formulation vehicle. For this purpose, a physical stability assessment of both forms in the suspension vehicle was assessed, with respect to sedimentation effects as well as with respect to physical form conversion. Results of suspension vehicle stability assessment are shown in Figure 12.

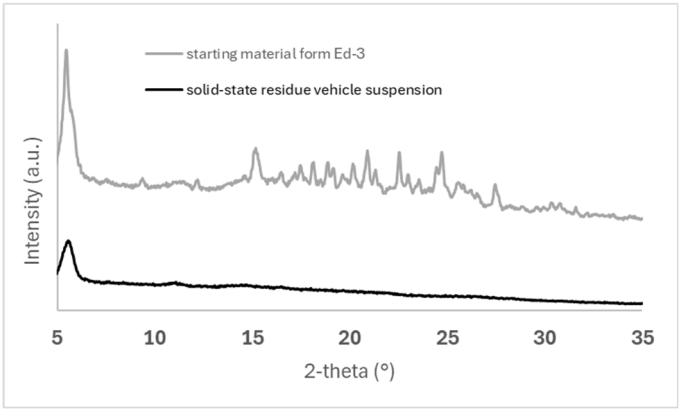

pH 24 h: 2.1

 doi:10.20944/preprints202603.2301.v1

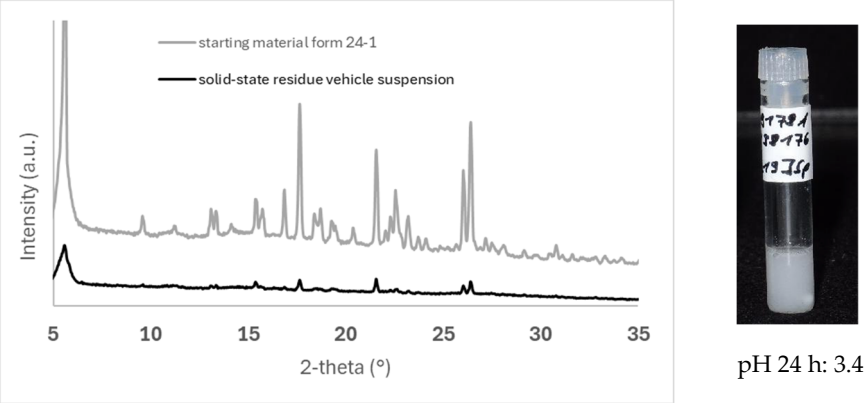

Figure 12. Stability assessment for co-crystal/salt forms in methocel/tween suspension vehicle (0.5% methocel, 0.25% tween-20 in water; target conc. 5 mg/mL free drug; unbuffered vehicle). top: 1,2-EDSA salt form - PXRD pattern on centrifuged residue after 24 h in suspension vs form Ed-3 (left); optical appearance of suspension after 24 h (right). bottom: 2,4-DHBA co-crystal form 24-1 - PXRD pattern on centrifuged residue after 24 h in suspension vs form 24-1 (left); optical appearance of suspension after 24 h (right).

While both crystal engineered forms yield a viually stable suspension regarding sedimentation effects up to 24 hours, only the 2,4-DHBA co-crystal form 24-1 is preserved as crystalline solid-state form in the suspension, whereas crystalline 1,2-EDSA hemi-salt for Ed-3 is shown to undergo phase conversion / salt hydrolysis to amorphous form (most likely amorphous free form). The higher reactivity of the salt form towards hydrolosis may be explained by two contributing factors when assuming that to very slight extent, dissolution of the solid-state form in the suspension vehicle will occur. Firstly, although protonation effect can be expected to be preserved into the diffusion boundary layer of the immersed solid of the salt, the attained pH-value in the diffusion layer is likely not reaching strongly acidic pH of 1.8 or lower (supported by pH-value of final suspension of 2.1), which would be required to stay below the anticipated pH-max of the salt (i.e., the pH-value below which the edisylate salt is thermodynamiclly stable, as typically the pH-max of a salt is approx. 1-2 pH-units below the pK_a [36]. And secondly, a higher local supersaturation in the diffusion boundary layer will be attained for the salt form due to stronger pH-shift in the diffusion layer compared to 2,4-DHBA co-crystal form, which then triggers precipiation of less soluble free amorphous form (as the more stable entity above assumed pH-max of the salt in the vehicle). Via such a mechanism, a subsequent conversion of the entire solid-phase can occur over repeated equilibrium processes.

2.4. Process Upscale of 2,4-DHBA Co-Crystal

A staged upscale approach was pursued for 2,4-DHBA-co-crystal form 24-1 as most promising solid-state form from crystal engineering study (sustained supersaturation effect vs amorphous free base, physically stable form in suspension vehicle for PK study):

- A small upscale at 80 mg scale was performed to provide sufficient material for an initial high-dose PK study in mice.
- Based on positive outcome of in-vivo exposure assessment of 2,4-DHBA co-crystal form 24-1 from said high-dose PK study in mice (see section 2.5), a further small g-scale upscale was performed to provide sufficient material for comprehensive in-vivo exposure behavior (e.g., dose escalation studies). To gain further understanding on the co-crystal formation step, the g-scale experiment was also monitored closely by Process-Analytical-Technology [PAT] tools in the g-scale reactor (in-situ video-microscopy [PARTICLEVIEW™], in-situ chord-length-distribution [PARTICLETRACK™]).

Results of upscale experiments for material provision for PK studies are summarized in Table 7. PAT data from g-scale upscale are shown in Figure 13. Although 80 mg scale process (multiple cooling/heating cycles 50-5 °C at 0.075 °C/min) and 1.7 g scale process (single cooling ramp 60-5 °C

 doi:10.20944/preprints202603.2301.v1

at 0.1 °C/min) were utilizing different process settings, both upscale experiments yield highly crystalline co-crystal form 24-1, with no hints for free excess 2,4-DHBA co-former being present (despite stoichiometric ratio co-former : API in 80 mg sample being very slightly over-stochiometric). This indicates a good robustness of the co-crystal formation step even without use of seed crystals. Residual solvent levels of crystallization solvent acetonitrile are well below ICH limit, regardless of an additional washing step being utilized (1.7 g scale) or not (80 mg scale). PAT data from 1.7 g scale experiment indicate that clear solution is obtained at 60 °C upon heating, and spontaneous nucleation upon cooling is observed at approx. 57 °C. Thus, the metastable zone width is presumably rather narrow, posing a challenge for a controlled seeding strategy. Initially formed primary particles appear to exhibit a slightly elongated shape, however, upon further cooling almost instantly formation of intergrown dendrite-like secondary particles is seen. Particle sizes of the 2,4-DHBA co-crystal final product are in the range 10 –100 µm based on square-weighted CLD data, with strongly isotropic-shaped particles due to the intergrown secondary particles. As a result, the material exhibits excellent filtration behavior.

Table 7. Summary of upscale experiments of 2,4-DHBA co-crystal form 24-1 for PK studies.

Scale[1]	Process details	Analytical data solid-state residue		
		Crystallinity[2]	Stoichiometry[3]	Residual solvents[4]
80 mg	▪ ~83 mg API in 8 mL acetonitrile ▪ addition of ~220 mg 2,4-DHBA at 50 °C ▪ 4 temperature cycles 50-5 °C at 0.075 °C/min ▪ Filtration, drying at 50 °C (N2 purge)	Crystalline, form 24-1 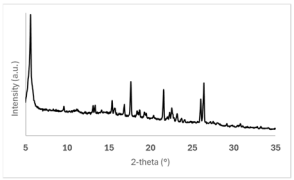	1.2 eq. 2,4-DHBA	MeCN 0.003 eq.
1.7 g	▪ ~1.675 g API in 185 mL acetonitrile ▪ addition of ~4.178 mg 2,4-DHBA at 60 °C ▪ cooling ramp 60-5 °C at 0.1 °C/min ▪ extended hold time at 5 °C for ~40 hours ▪ Filtration, washing with n-heptane, drying at 50 °C (N2 purge)	Crystalline, form 24-1 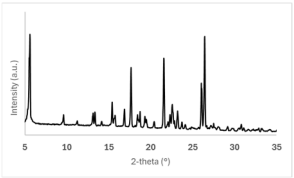	1.0 eq. 2,4-DHBA	MeCN 0.0007 eq. / n-heptane [5] 0.0005 eq.

[1] Free base quantity, [2] Powder X-Ray Diffraction, [3] ^{1}H-NMR or IC (chloride), [4] ^{1}H-NMR, [5] washing medium.

43 °C / cooling ramp: dendritic growth

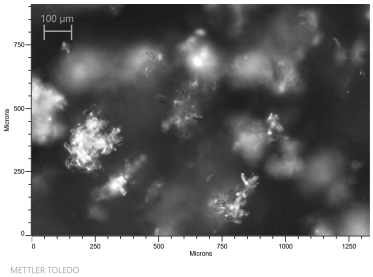

5 °C / end of final hold step: dendrites

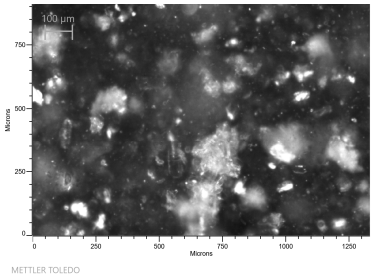

 doi:10.20944/preprints202603.2301.v1

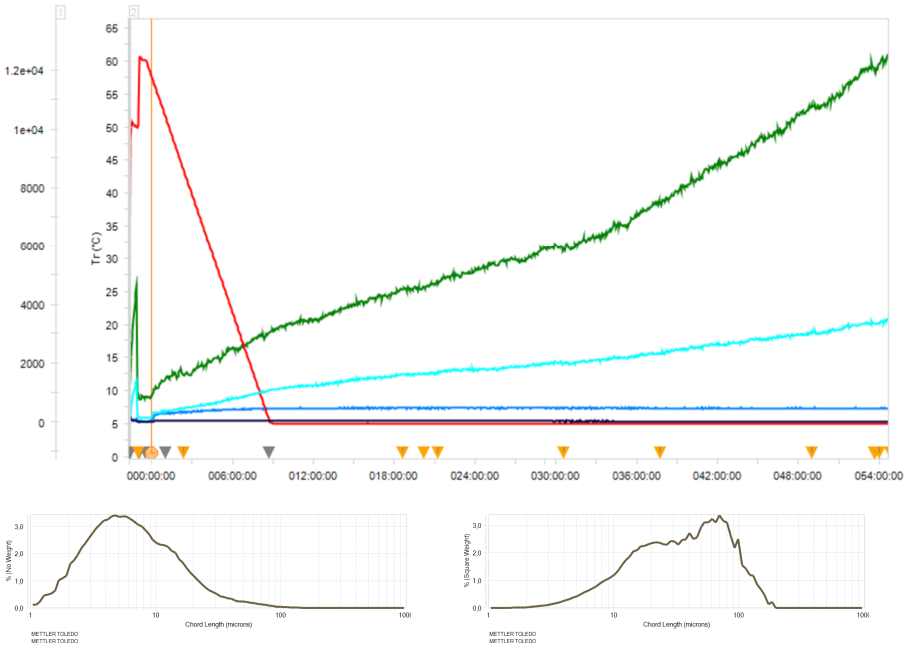

Figure 13. PAT data of g-scale upscale experiment of 2,4-DHBA co-crystal form 24-1. top: PARTICLEVIEW™ images at various stages of crystallization process. middle: reaction temperature (red) vs particle counts from PARTICLETRACK™ (green: total counts, light blue: counts 10-50 µm, blue: counts 50-150 µm, dark blue: counts 150-300 µm). bottom: Chord Length Distribution (CLD) at end of 5 °C holding time (left: non-weighted, right: square-weighted).

2.5. In-Vivo Oral PK Study of 2,4-DHBA Co-Crystal in Mouse

Results of oral high-dose PK study in mouse of 2,4-DHBA co-crystal form 24-1 in comparison with free base amorphous form are summarized in Table 8. Corresponding plasma concentration profiles over time are displayed in Figure 14:

Table 8. Mouse oral high-dose PK data for MSC178 amorphous free form vs crystalline 2,4-DHBA co-crystal (suspension vehicle methocel/tween [0.5% methocel, 0.25% tween-20 in water], 5 mg/mL[1], 50 mg/kg[1], mean data from n=3 animals for each form).

Solid-state form	tmax	Cmax	AUC_{μ}[2]
free base amorphous form	6 h	1750 ng/mL	32800 h*ng/mL
2,4-DHBA co-crystal form 24-1	0.5 h	5290 ng/mL	77500 h*ng/mL

[1] Amounts referred to free base entity in all cases, [2] 0-24 h, AUC to infinity is not reported because of large (>20% of measured AUC) extrapolated AUC.

 doi:10.20944/preprints202603.2301.v1

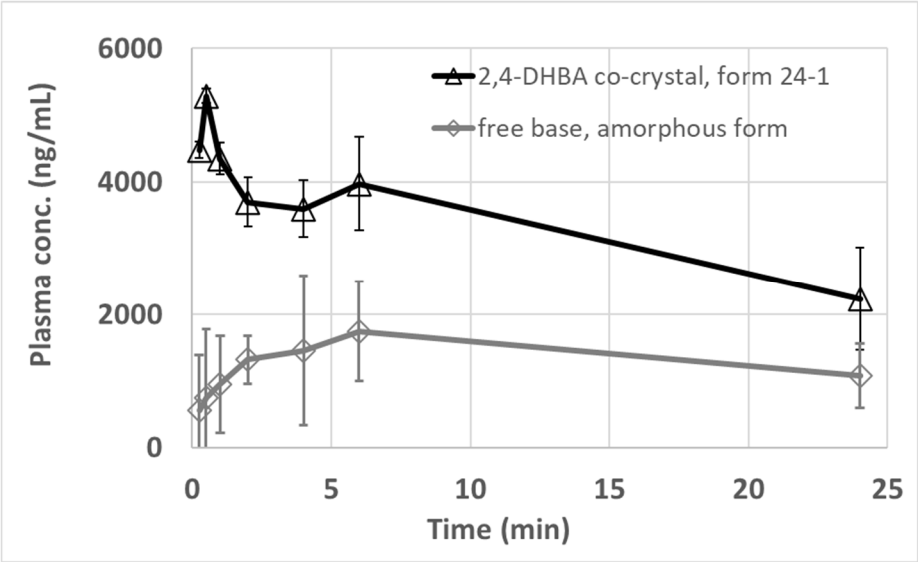

Figure 14. Plasma concentration–time profiles from oral high-dose PK study in mice. (Suspension vehicle used was methocel/tween [0.5% methocel, 0.25% tween-20 in water], 5 mg/mL, 50 mg/kg free base, data points represent mean data ± SD from n=3 animals for each form. Experimental details for the in vivo PK study and bioanalytical method used for MSC178 quantification can be found in Materials and Methods section.).

The oral high-dose (50 mg/kg free base) PK data in mouse displayed on Figure 14 and in Table 8 clearly show that the total exposure [AUC0-24h] observed after dosing as a suspension in methocel/tween [0.5% methocel, 0.25% tween-20 in water] of the 2,4-DHBA co-crystal form 24-1 is clearly higher (2.36-fold) than the amorphous free form of MSC178. The absorption kinetics and extent are also clearly different with a rapid (0.5h versus 6h) tmax and higher Cmax (3.0-fold difference) observed for the 2,4-DHBA co-crystal form 24-1 as compared to the amorphous free form of MSC178. The data displayed on Figure 14 also show that the inter-animal variability in mouse is smaller (error bars, SD n=3) after oral dosing with the 2,4-DHBA co-crystal form 24-1 of MSC178 as compared to its amorphous free form.

3. Discussion

This study shows the interesting phenomenon that crystalline forms (either salt or co-crystal) dissolve faster and supersaturate higher than amorphous form of free base. Moreover, in contrast to common perception and literature data showing higher solubility and dissolution effects of salts vs co-crystals [37,38], this study shows a higher and more sustained supersaturation effect for a co-crystal compared to a salt form. A salt form can overcome solubility constraints by protonation effect in diffusion layer, however, for such poorly basic compounds this is no sustained effect and high risk of deprotonation in less acidic milieu [36,39], which could also be seen in the instability of 1,2-EDSA salt in the formulation vehicle. Co-crystals do not offer the potential of improved hydration layer interaction via protonated charged drugs in diffusion layer. This can also be seen in 3,4-DHBA co-crystal which does not provide any dissolution and supersaturation benefit vs amorphous free form (or rather a potential improved solubilization benefit in aqueous hydration layer may be so small to just compensate for the additional energy barrier of lattice energy in the 3,4-DHBA co-crystal vs the amorphous free form). In contrast, the 2,4-DHBA co-crystal exhibits a pronouncedly higher dissolution and supersaturation profile compared to amorphous free from. This strikingly different behavior of both co-crystals, despite structurally very similar co-formers being utilized, may be explained by various contributions:

- As shown by Good et al. [40], there is a solubilizing effect of co-former on the solubility of co-crystal, showing that co-crystal solubility often is proportional to solubility of the respective co-

 doi:10.20944/preprints202603.2301.v1

former. Based on higher solubility data of 2,4-DHBA vs 3,4-DHBA in organic solvents as shown before, this may also facilitate higher supersaturation levels in aqueous media.

- Competitive processes between attraction of taurocholate from the dissolution medium vs attraction of water to crystal surfaces play a critical role for understanding dissolution and supersaturation behavior in co-crystals, as shown by Chen et al. [41]. Precipitation of free form without built-up supersaturation levels may occur if very fast selective dissolution of the co-former occurs from the co-crystal lattice. Preferred coordination of taurocholate on crystal faces can effectively slow down such a rapid dissolution of co-former alone. The pronouncedly stronger surface hydrophilicity in 3,4-DHBA co-crystal compared to 2,4-DHBA co-crystal (expressed in both higher total water-specific surface area equivalent as well as higher surface hydrophilic ratio), explains the absence of any supersaturation effect in the non-sink dissolution compared to the 2,4-DHBA co-crystal, as the 2,4-DHBA co-crystal can more effectively coordinate taurocholate molecules on crystal faces upon dissolution process, whereas for the 3,4-DHBA co-crystal water adsorption is more preferred, resulting in fast release of co-former and fast precipitation of free form. The single crystal structure of the 3,4-DHBA co-crystal indicates that the parallel chains formed by the API and the co-former, along with the hydrophilic channels running parallel to them, may facilitate the dissociation of the conformer pair more effectively than in the 2,4-DHBA co-crystal, where the DHBA homosynthons are enclosed by API molecules. The notable difference in aqueous solubility between 3,4-DHBA (18 mg/mL) and the API (<10 µg/mL) facilitates the preferential separation of 3,4-DHBA from the lattice of the 3,4-DHBA co-crystals. As a result, an unstable, high-energy amorphous API is generated. Over time, the API concentration surpasses its equilibrium solubility, prompting the transformation of the amorphous API into stable API crystals, in accordance with Ostwald's law of stages. This process leads to the precipitation of the API. Additionally, any excess 3,4-DHBA that exceeds its equilibrium solubility will also precipitate, ultimately causing the dissociation of the 3,4-DHBA co-crystal [42]. A fast preferential dissolution of 2,4-DHBA from the 2,4-DHBA co-crystal form 24-1 and subsequent precipitation of free form, is effectively inhibited and slowed down due to the surface chemistry differences of co-crystal particles.

The same rationale can explain the higher and more sustained supersaturation level in 2,4-DHBA co-crystal compared to 1,2-EDSA salt form, which also exhibits a much higher surface hydrophilicity (in this case, however, other mechanisms such as protonation effect of the API in the dissolution layer additionally contributes to the supersaturation effect of the salt). The exceptional low surface hydrophilicity in 2,4-DHBA co-crystal is also highlighted in comparison with free base amorphous form, which shows a higher surface hydrophilicity despite lack of any polar co-former molecules in the structure. This emphasizes the strong contribution of this aspect explaining the sustained supersaturation effect of the 2,4-DHBA co-crystal form.

- The overall dense packing arrangement in the crystal structure of 2,4-DHBA co-crystal, including multiple interactions involving the 2,4-DHBA co-former molecules in the structure, counter-acts a fast and selective dissolution process of the acid, whereas in 3,4-DHBA co-crystal, the water-accessible void structures and proximity of 3,4-DHBA co-former to these voids via the para-hydroxyl group may ease such a dissolution process of co-former moiety alone.
- Another hypothesis may be that a stronger interaction between API molecule and the co-former may persist also in the solution phase of the 2,4-DHBA co-crystal (compared to solution phase of 3,4-DHBA co-crystal), which may potentially inhibit direct nucleation and precipitation of free API from supersaturated solution state. Such solution-state interactions were shown by NMR data supersaturation mechanisms for API – polymer interactions [43], however, in case of MSC178 co-crystals, first NMR experiments revealed far too low concentrated solutions in aqueous media to detect any API signals. The same holds true for Raman spectroscopic investigations by Transmission Raman spectrometer on the FaSSIF solutions, which did not yield any API signals due to insufficient concentration levels of dissolved API (NMR and Raman data not shown here). Attempts to derive solution-interaction strength of API-co-formers for 2,4-

 doi:10.20944/preprints202603.2301.v1

DHBA and 3,4-DHBA co-crystals were made based on thermal analysis data after melting (representing a liquidus-phase without any solvent), however, such data would be somewhat artificial, as no competitive effect of the aqueous milieu and taurocholate environment are reflected. Moreover, even bearing this in mind, degradation onsets from TGA heating scans in liquidus phase (as measure for liquidus phase interaction strength) do not support a stronger interaction between API to 2,4-DHBA compared to interaction between API to 3,4-DHBA (TGA data not shown here). Hence, there is no direct evidence for a potential stronger API – co-former interaction in solution phase of 2,4-DHBA co-crystal. The observed heat capacity differences in solid state between 2,4-DHBA co-crystal and 3,4-DHBA co-crystal suggests slightly lower molecular mobility in solid-state and lower solid-state entropy for 2,4-DHBA co-crystal. This in combination with the higher melting point in 2,4-DHBA co-crystal form 24-1 suggests stronger lattice interactions between API and co-former in this form. This may contribute to a stronger initial interaction in the diffusion layer, potentially also strengthened by the aromatic interactions between API and 2,4-DHBA as observed in the crystal structure. Overall, however, the lower surface hydrophilicity as discussed before is more likely to be the key mechanism to explain the supersaturation effect of the 2,4-DHBA co-crystal.

- The lower surface hydrophilicity in 2,4-DHBA co-crystal form 24-1 compared to co-crystal form 34-1 is also confirmed by the crystal morphologies as calculated by BFDH method, showing mainly hydrophobic functional groups being present in dominant crystal faces of 2,4-DHBA co-crystal form 24-1 (pyrazole and fluoropyridines), whereas polar hydroxyl groups are present in main crystal faces of 3,4-DHBA co-crystal form 34-1.

The comprehensive characterization data of both identified co-crystals (2,4-DHBA co-crystal vs 3,4-DHBA co-crystal) shows that for attaining high-supersaturating co-crystals, it is not sufficient to focus solely on reducing lattice energy by disrupting crystal lattice interactions (i.e., to overcome “brick-stone”-like properties), but to also look into adequate solubilizing behavior in the quaternary interaction API – co-former – bio-surfactant (taurocholate) – water. As to certain extent a stronger co-former coordination within the co-crystal lattice may even be beneficial (to avoid fast and selective co-former dissolution from the co-crystal matrix), it may be concluded that a sweet spot in terms of solid-state interactions within the co-crystal lattice must be met.

In contrast to 2,4-DHBA co-crystal, 1,2-EDSA salt undergoes phase conversion in the suspension vehicle. Although the stronger pH-shift impact upon dissolution in the diffusion layer of the 1,2-EDSA salt, triggering higher supersaturation and subsequently precipitation of free form, will strongly contribute to this conversion (as discussed in section 2.3.2.), a further root-cause can be derived as well from differences in surface chemistry of crystal faces in the 1,2-EDSA salt compared to crystal faces in the 2,4-DHBA co-crystal. Sorption data confirm that 2,4-DHBA cocrystal exhibits pronouncedly lower water-specific surface area equivalent and surface hydrophilic ratio compared to 1,2-EDSA salt. Like what was discussed for impact of taurocholate coordination on crystal faces for the dissolution and supersaturation mechanism, competitive process on particle surface between water and excipient molecules from the vehicle (methocel, tween) will also play a vital role in stability behavior in the suspension vehicle. Therefore, a stronger affinity of associated crystal faces in the 2,4-DHBA co-crystal to the less hydrophilic excipient molecules (relative to adsorption affinity of water molecules) can be assumed, compared to the 1,2-EDSA salt which clearly bears more hydrophilic surface domains. Even in case of hardly any dissolution occurring into the diffusion layer in the suspension vehicles, the higher water affinity in 1,2-EDSA salt on crystal surfaces can facilitate dissociation in surface layers, which can act as seeds for adjacent layers in crystals to undergo bulk hydrolysis. Interestingly, high water affinity in 1,2-EDSA salt is not an intrinsic feature of the protonated salt form being present, as the 3,4-DHBA co-crystal also exhibits higher surface hydrophilic ratio than 2,4-DHBA co-crystal. Although water activity and affinity to water vapor uptake on solids was demonstrated as being a directly correlating factor with disproportionation effects in salt forms [44], the findings for 3,4-DHBA co-crystal clearly suggest that surface

 doi:10.20944/preprints202603.2301.v1

hydrophilicity is not driven by the per se presence or absence of ionic interactions in the crystal lattice, but rather a consequence of surface chemistry in most dominant crystal faces in each solid-state form.

Small g-scale upscale of 2,4-DHBA co-crystal revealed a low extent of anisotropic growth in primary particles. This can be explained by the extended multi-dimensional hydrogen bonding network as well as additional aromatic interactions being present in the 2,4-DHBA co-crystal form 24-1 crystal structure. On molecular level, multiple options persist for molecules in solution to attach to the surfaces of first nuclei and crystals. This may also explain the high tendency for formation of intergrown dendrite-like secondary particles as orthogonal growth directions can be realized when attaching via different molecular coordination motives. The obtained particle sizes from combination of primary and secondary particle growth are in an ideal window to avoid sedimentation in the suspension vehicle (if too large particles) and to avoid agglomeration (if too small particles). Moreover, the fractal particle surface structure in the intergrown secondary particles may help to avoid agglomeration (less particle-particle contact area) and may be beneficial to avoid pronounced surface wettability to trigger dissociation (as also seen in low total water-specific surface area equivalent). It must be emphasized that these favorable particle properties are already achieved without any crystallization process optimization, and further options are possible to additionally gain control on crystallization process with respect to primary particle size distribution and particle shape (e.g., by more elaborated defined seeding strategies). Even without further optimization, the favorable secondary particle properties are anticipated to result in excellent powder processing properties (such as good flowability, high bulk density), highlighting once again the potential of co-crystal forms also in context to improve manufacturability aspects [45]. The g-scale manufactured 2,4-DHBA co-crystal and its inherent particle properties would allow also usage in more sophisticated formulation vehicles such as Powder-In-Capsules for higher species animal PK studies.

The in vivo PK data corroborate the physical chemistry profile of the different solid forms which were characterized and described in the previous sections of this paper, showing that (a) the 2,4-DHBA cocrystal form 24-1 of MSC178 is stable in the oral methocel/tween vehicle used in the study and (b) that the non-sink dissolution profile differences in biorelevant intestinal medium (FaSSIF) of the 2,4-DHBA cocrystal form 24-1 vs amorphous form of MSC178 translate perfectly well into observed PK exposure differences of both forms (2.4-fold in-vivo exposure increase of co-crystal form 24-1 vs amorphous free form [based on $AUC_{0\text{-}24h}$ data in PK study] in comparison with 2.3-fold in-vitro supersaturation increase of co-crystal form 24-1 vs amorphous free form [based on $AUC_{0\text{-}120min}$ data in non-sink dissolution profiles] .

It is interesting to observe that predicted molecular hetero dimer excess enthalpies form based on COSMOQUICK calculations for both co-crystal forms (2,4-DHBA co-crystal form 24-1, 3,4-DHBA co-crystal form 34-1) match in rank order with the experimentally observed dissolution / supersaturation effects (i.e., the more negative the calculated excess enthalpy, the higher the supersaturation behavior). Although this may on first glimpse be counter-intuitive, this was also observed in literature for COSMO-RS predictions (interaction strength API – co-former) in combination with MD calculations (mean-distance API – co-former in aqueous media), overall postulating that co-former with high-excess-energy in predicted co-crystal interaction can effectively compete with water for interactions with the API and inhibit nucleation [46]. The current study suggests that a far less complex approach utilizing simplified excess enthalpy assessment based on COSMOQUICK fragmentation approach may suffice to predict also best co-formers to achieve supersaturation effects. However, more comprehensive and systematic work would be needed to substantiate this.

Moreover, internally developed algorithms on co-crystal formation likelihood were examined on the system. These algorithms combine computational chemistry to calculate interaction features, such as excess enthalpy, free energy of mixing, shape fitting parameters and solubility of API in co-former with machine learning algorithms trained on a sufficient experimental database and yield a score on the co-crystal formation likelihood ranging from 0 to 1 [47]. These calculations show an even more discriminating effect between 2,4-DHBA- and 3,4-DHBA-co-crystals for MSC178 (predicted co-

 doi:10.20944/preprints202603.2301.v1

crystal formation score factor 2.5 higher for 2,4-DHBA co-crystal than for 3,4-DHBA co-crystal, compared to factor 1.3 higher excess enthalpy for 2,4-DHBA co-crystal vs 3,4-DHBA-co-crystal from COSMOQUICK). The higher score of 2,4-DHBA compared to 3,4-DHBA is related to the difference in excess enthalpy and differences in molecular descriptors, such as the H-bond acceptor strength, entropic contributions, chemical potential and σ-profiles in general. This indicates that the internally developed co-crystal prediction tool may also provide better discriminative power for co-crystal performance aspects such as supersaturation. Again, more systematic work is suggested to substantiate these observations.

4. Materials and Methods

Materials

API free base material for crystal engineering study was obtained from Medicinal Chemistry laboratories, following synthetic routes as described by Burgdorf et al. [7]. Different lab-scale batches from same synthetic route were used for solubility and crystal engineering experiments, all with purity levels of at least 98% a/a (based on generic HPLC method from synthesis labs).

High-purity p.A.-grade solvents were used for solubility and crystallization experiments (1,4-dioxane: Merck KGaA LiChrosolv, cat.-no. 1.03132; acetonitrile: Merck KGaA LiChrosolv cat.-no. 1.00030; ethyl acetate: Merck KGaA Emsure cat.-no. 1.09623).

2,4-dihydroxybenzoic acid was obtained from SAFC (cat. no. 102698557, purity 97%). 3,4-dihydroxybenzoic acid was obtained from Thermo Scientific (cat. no. B24016.14, purity 97%). 1,2-ethandisulfonic acid dihydrate was obtained from Thermo Scientific (cat. no. 384800050, purity 98%). Hydrochloric acid was purchased from VWR as 32% aqueous solution (cat.-no. 20259.310), and diluted 1:10 in water prior to addition to crystallization trials.

In-silico assessment of suitable co-formers for salts and co-crystals

Excess enthalpy (H_{ex}) calculations of molecular hetero dimers API : co-former relative to molecular homo-dimers API : API and co-former : co-former, respectively, were calculated in software COSMOquick (C. Loschen, A. Hellweg, A. Klamt, COSMOquick, Version 1.3; COSMOlogic GmbH & Co. KG, Leverkusen, Germany, 2014). H_{ex} levels were calculated at 298 K for a 1:1 stoichiometry.

Solubility assessment of MSC178 and solid co-formers

Solubility estimation of MSC178 and solid co-formers 1,2-EDSA, 2,4-DHBA, and 3,4-DHBA were performed at room temperature using the incremental solvent addition method. For this, defined quantities of respective solid material was accurately weighed into 1.5 mL glass vials with tight screw caps , and magnetic stirring bars were added. Vials were placed on a multi-position stirring plate at room temperature (20-25 °C) and agitated. Solvent was increment-wise added to the pre-weighted defined quantities of solid material in steps of 50 µL up to total volumes of 300 µL, and in steps of 100-250 µL until total max. volumes of 1.5 mL were reached. After each solvent addition step, vials were tightly closed again, and equilibration of dispersions under stirring was allowed for at least 15 min. In case undissolved solid residues were visually identified after each solvent addition step, further solvent increments were added acc. to above solvent addition process until a visually clear solution was obtained.

mg-scale salt- and co-crystal formation trials

Approx. 15-20 mg starting material MSC178 (amorphous form) were dispersed into 1.5 mL ethyl acetate or 1.7 mL acetonitrile, respectively, in 4 mL glass vials with tightly closed screw caps. Magnetic stirring bars were inserted into dispersions, and vials were placed in a custom-made multi-position thermos-block, which was placed on a magnetic stirrer (IKA RCT basic). The thermo-block was attached to a programable cryostat (Huber petite fleur line). Dispersions were heated to 50 °C under gentle stirring to obtain visually almost clear solutions at 50 °C. Excess quantities of respective solid co-former were used reflecting the solubility ratio of MSC178 vs co-former in respective solvent. Respective calculated excess quantities of solid-co-formers were weighed and added to respective heated dispersions. In case of HCl, approx. 1.1 eq. of stock solution made from 1:10 dilution of 32%

 doi:10.20944/preprints202603.2301.v1

aqueous HCl solution was accurately pipetted to the warm solution of MSC178. Solutions or (in case of spontaneous precipitation after addition of co-former) dispersions were cooled down from 50 °C to 4 °C in 10 h using a linear cooling ramp, followed by re-heating to 50 °C in 1 h. This cooling/heating cycle was repeated four times, followed by a final slurry agitation step at 4 °C for at least 2 h. Final suspension samples were solid/liquid-separated by centrifugation (Eppendorf 5810R) at 12,000 rpm. Supernatant solutions were pipetted off and discarded. Wet solid residues were gently dried under nitrogen purge at room temperature for at least 1 h.

For miniaturized upscales, experiments were set-up analogously using approx. 45-80 mg starting material MSC178 (amorphous form) and respective scaled larger quantities of solvent and co-formers. 45 mg upscale trials were performed in 8 mL glass vials with tightly closed screw caps, using a second custom-made multi-position thermos-block with larger cavities to host the larger vials. For edisylate salt and 3,4-DHBA co-crystal, slight variation in stochiometric quantities being used were adapted based on results of co-former equivalents retrieved in solid samples of initial 15 mg trials.

Experimental details of utilized quantities in mg-scale screening trials are summarized in Table 9.

Table 9. Experimental details of mg-scale co-crystallizations experiments.

Co-former	Solvent / target stoichiometry	Quantities to set-up experiments		
		MSC178	Solvent	Co-Former
HCl	ethyl acetate / 1:1	15.8 mg	1.5 mL	40 µL 1:10 dilution
	acetonitrile / 1:1	15.8 mg	1.7 mL	40 µL 1:10 dilution
	acetonitrile / 1:1	46.9 mg	5.2 mL	131 µL 1:10 dilution
1,2-EDSA	ethyl acetate / 1:1	16.4 mg	1.5 mL	9.2 mg
	acetonitrile / 1:1	16.3 mg	1.7 mL	9.0 mg
	ethyl acetate / 1:1	48.1 mg	4.5 mL	35.9 mg
	ethyl acetate / 0.5:1	49.8 mg	4.5 mL	17.8 mg
2,4-DHBA	ethyl acetate / 1:1	15.7 mg	1.5 mL	51.2 mg
	acetonitrile / 1:1	16.2 mg	1.7 mL	42.0 mg
	acetonitrile / 1:1	45.8 mg	5.0 mL	134.5 mg
	acetonitrile / 1:1	83.0 mg	8.0 mL	220 mg
3,4-DHBA	ethyl acetate / 1:1	17.3 mg	1.5 mL	62.3 mg
	acetonitrile / 1:1	16.9 mg	1.7 mL	13.2 mg
	acetonitrile / 1:1	48.4 mg	5.0 mL	23.5 mg

[1] Powder X-Ray Diffraction, [2] ^{1}H-NMR or IC (chloride), [3] ^{1}H-NMR.

Process upscale of 2,4-DHBA co-crystal

Upscale of 2,4-DHBA co-crystal was performed in 1.7 g scale in an EasyMax crystallization platform in 400 mL reactor and overhead 3-bladed propeller stirrer with blades upwards (EasyMax 402, Mettler-Toledo GmbH). A Mettler-Toledo ParticleTrack™ (FBRM G400) probe and a Mettler-Toledo ParticleView™ (PVM19) probe as well as a Mettler-Toledo Pt100 temperature sensor were immersed as PAT probes in the reactor through the PTFE reactor lid. 1.675 g of MSC178 amorphous form were suspended in 185 mL acetonitrile and agitated at 400 rpm. The suspension was heated in the EasyMax reactor to 50 °C and held for approx. 60 min, still yielding a slightly residual turbid suspension. 4.178 g of 2,4-DHBA were added as solid, and suspension was heated to 60 °C at 10 K/min to obtain a clear solution, followed by a 30 min hold time at 60 °C. Solution was then cooled 60 °C to 5 °C at 0.1 K/min. Final suspension obtained at 5 °C was agitated at 5 °C for a prolonged hold time for approx. 40 hours to allow crystal growth. The suspension was filtered via a vacuum filtration unit with a cellulose paper filter. Wet filter cake was washed with approx. 10 mL n-heptane (p.A. grade), and subsequently dried under nitrogen purge at room temperature.

 doi:10.20944/preprints202603.2301.v1

Reaction control as well as data analysis of PAT trends was done in iControl software (ver. 6.0.53) interfaced to iC FBRM software (ver. 4.4.33) and iC PVM software (ver. 7.0.188), respectively (all from Mettler-Toledo GmbH).

Powder X-Ray Diffraction

Samples (solids as well as suspensions from vehicle stability assessment) have been prepared in a combinatorial 96-well-plate (comprising an X-ray amorphous foil as bottom). Measurements have been performed in transmission geometry with Cu-Kα1 radiation on a Stoe StadiP 611 diffractometer equipped with a Mythen detector. Scans were recorded from 0-36° 2θ simultaneously (step width of 0.03° 2θ, 30 seconds per step). Diffraction data were exported to Microsoft Excel for creation of diffraction pattern plots.

Differential Scanning Calorimetry

Samples were investigated on a Mettler-Toledo heat-flux Differential Scanning Calorimeter DSC1 with autosampler, using a nitrogen inert gas atmosphere (50 mL/min). Overview scans were carried out in Al 40 µL pans with open lids from 25-250 °C at 5 °C/min (sample weights of 2-5 mg. Modulated DSC (mDSC) was performed in Al 40 µl pans (sample weights 3-8 mg) with centering pins and laser-perforated 50 µm pinhole via Mettler-Toledo TOPEM™ technology with stochastic temperature modulation, using a linear heating rate of 1 K/min from 25-75 °C, a temperature amplitude of 1K, and a stochastic modulation phase between 15 – 45 s, respectively. Heat capacity profiles were calculated from reversing heat-flow after Fourier Transformation in Mettler-Toledo STARe software ver. 16.0. Weights of Al sample and reference pans were used as heat capacity refences. Duplicate preparations were measured each on two different samples of each solid-state form.

Gravimetric Vapor Sorption (water vapor sorption)

Samples were weighed into disposable Al pans and placed on the sample position of the GVS instrument with microbalance and incubator (DVS-Intrinsic, Surface Measurement Systems, SMS). A nitrogen overall flow rate of 200 mL/min (combined dry and humid stream) was used for humidification. Milli-Q water from internal supply pipes was used in water reservoir. Water vapor sorption isotherms were acquired at 25 °C, using an adsorption segment from 0%RH to 98%RH (with 10%RH steps and a final 8%RH step, respectively), and a final desorption segment from 98%RH to 0%RH (with an initial 8%RH step and 10%RH steps, respectively). RH levels were set-up based on mass flow regulators. For all RH steps, an equilibrium condition of dm/dt ≤0.0005 wt%/min was used, with a minimum RH step time of 10 minutes and a maximum RH step time (timeout) of 360 minutes. Isotherms were calculated from final weight readings at end of each kinetic equilibration step and referenced to dry weight from end of 0% RH step. Sorption isotherms were plotted in Microsoft Excel using DVS Standard Analysis Suite (ver. 7.1.0.25) from SMS.

Additional water vapor sorption data were acquired with higher RH resolution in lower partial pressure range, using an initial drying step at 0% RH for 240 min followed by adsorption segment 5-50% RH in steps of 5% RH. For all RH steps, an equilibrium condition of dm/dt ≤0.0005 wt%/min was used, with a minimum RH step time of 10 minutes and a maximum RH step time (timeout) of 360 minutes. Low partial-pressure isotherms were calculated acc. to Excess Surface Work (ESW) sorption model as described by Adolphs et al. [28] based on chemical potential changes Δμ and calculated Excess Surface Work (ESW) term φ upon adsorption process:

(1) $\Delta\mu = RT \cdot ln\frac{p}{p_s}$

(2) $\varphi := n_{ads} \cdot \Delta\mu$

ESW term φ was normalized twice by (a) dividing ESW by molar quantity of sorbed water in the minimum of ESW plot, and (b) by dividing normalized ESW by product of universal gas constant R multiplied with temperature T:

(3) $\varphi_{notm1} = \frac{\varphi}{n_{ads_{min}}}$

(4) $\varphi_{notm2} = \frac{\varphi_{norm1}}{RT}$

 doi:10.20944/preprints202603.2301.v1

These normalization procedures reduce the y-axis to a dimensionless scale which reveals the loss of degrees of freedom upon sorption process.

For each normalized ESW plot, a minimum point is obtained. This minimum point can be interpreted as RH where strongest interaction of adsorbed water vapor with powder surface is realized and hence is resembling an equivalent of maximum primary surface coverage of water vapor (at lower RH below minimum point, full coverage of primary hydrophilic surface domains by water vapor is not yet realized; at higher RH above minimum point, increasing multilayer sorption decreases the overall sorption energy). Consequently, adsorbed molar quantity in the minimum point of normalized ESW function, $n_{ads_{min}}$, can be re-calculated into a water-specific surface area equivalent (to account for surface area domains that can realize maximum sorption energy upon adsorption of water vapor) using Avogadro constant and mean cross-sectional area of a single water molecule (10^{-20} m²/molecule). For each solid-state form under investigation, ESW sorption data were acquired from two measurements. ESW sorption model was plotted and evaluated in Microsoft Excel based on exported GVS data from the measurement instrument.

Organic Vapor Sorption (n-octane sorption)

Samples were weighed into disposable Al pans and placed on the sample position of the OVS instrument with microbalance and incubator (DVS-Advantage, Surface Measurement Systems, SMS). A nitrogen overall flow rate of 200 mL/min (combined dry and humid stream) was used for organic vapor generation. N-octane sorption isotherms were acquired at 25 °C in partial pressure (p/p_s) range 0-50%with 10% p/p_s steps., using n-octane extra pure solvent (Acros Organics, cat.-no. 129375000). Prior to n-octane sorption steps, equilibration under dry nitrogen (0% p/ps) was performed for 240 min. N-octane levels were adjusted by feedback loop (closed loop) from Dew Point Analyser (DPA) sensor readings. For all n-octane sorption steps, an equilibrium condition of dm/dt ≤0.0005 wt%/min was used, with a minimum step time of 10 minutes and a maximum step time (timeout) of 360 minutes. Resulting n-octane gravimetric sorption data were evaluated for n-octane-based specific surface area (SSA) acc. to BET model in Microsoft Excel using DVS Advanced Analysis Suite (ver. 7.1.0.25) from SMS, in the partial pressure range 5-30% p/p_s using a mean cross-sectional area of a single n-octane molecule of 63 Ă²/molecule [5, Williams].

Single crystal X-Ray Diffraction

Single crystals of the 2,4-DHBA co-crystal were selected and mounted on a XtaLAB Synergy R, HyPix-Arc 150 diffractometer. The crystal was kept at 99.9(5) K during data collection. The instrument was operated and the diffraction data were processed in the program CrysAlis^{Pro}.[Rigaku Oxford Diffraction, CrysAlis^{Pro} software system, Rigaku Corporation, Wrocław, Poland, 2025 (version 1.171.44.117a] Using Olex2 [48] the structure was solved with the SHELXT [49] structure solution program using Intrinsic Phasing and refined with the SHELXL [49] refinement package using Least Squares minimization. All non-hydrogen atoms were refined through anisotropic displacement parameters, and all non-protic H-atoms were geometrically positioned and refined as riding. Protic H-atoms bound to heteroatoms were assigned by residual electron density. The CF_3 group is disordered over two positions and was refined using a disorder model with respective occupancies of 0.57/0.43.

Crystal Data for the 2,4-DHBA cocrystal (merged): CCDC: 2540221, $C_{26}H_{19}F_4N_7O_5$, M =585.47 g/mol, triclinic, space group *P*-1 (no. 2), a = 8.3301(4) Å, b = 10.0638(4) Å, c = 15.9928(7) Å, α = 80.955(4)°, β = 77.931(4)°, γ = 84.053(4)°, V = 1291.30(10) Å3, Z = 2, T = 99.9(5) K, μ(Cu Kα) = 1.095 mm-1, Dcalc = 1.506 g/cm3, 20556 reflections measured (5.706° ≤ 2Θ ≤ 149.866°), 5057 unique (Rint = 0.0352, Rsigma = 0.0407) which were used in all calculations. The final R1 was 0.0461 (I > 2σ(I)) and wR2 was 0.1197 (all data).

Single Crystal Structure Determination via 3D Electron Diffraction

(General remarks) Electrons feature very strong interactions with the electrostatic potential of atoms. Subsequently, electron diffraction allows for performing experiments with crystallites in the nanometer range. However, it needs to be considered that the absorption of the samples is much stronger and the data are affected by dynamical diffraction as well as ionic scattering factors

 doi:10.20944/preprints202603.2301.v1

compared to X-ray diffraction. This can lead to seemingly bad R-values for the refinement in the simplistic kinematic approximation.

Microcrystalline powder of the 3,4-DHBA co-crystal was spread on a lacey-carbon-supported copper TEM grid. Colorless crystallites with a few 100 nm thickness were selected for 3D-ED/microED measurements. Cryo-transfer, i.e., freezing of samples prior to introduction to vacuum, at 100 K using a Gatan ELSA (Model 698) specimen holder was applied here.

Electron diffraction measurements were collected using the Rigaku XtaLAB Synergy-ED, equipped with a Rigaku HyPix-ED detector optimized for operation in the continuous rotation 3D-ED experimental setup [50,51]. Data acquisition was performed at 100 K under high vacuum with an electron wavelength of 0.0251 Å (200 kV). The instrument was operated and the diffraction data were processed in the program CrysAlis^{Pro}. .[Rigaku Oxford Diffraction, CrysAlis^{Pro} software system, Rigaku Corporation, Wrocław, Poland, 2025 (version 1.171.44.117a] A multi-scan absorption correction was performed using spherical harmonics implemented in SCALE3 ABSPACK scaling algorithm in CrysAlis^{Pro}. The structure was solved using ShelXT, [49] and subsequently, refined with kinematical approximation using ShelXL [49] in the crystallographic program suite Olex2.[Rigaku Oxford Diffraction, AutoChem 7 software system in conjunction with OLEX2, Rigaku Corporation, Wrocław, Poland, 2025 (version 1.5-ac7-018).] By merging data of four individual grains/datasets, a completeness of 99.6% up to a resolution of 0.80 Å was achieved. All non-hydrogen atoms were refined through anisotropic displacement parameters, and all non-protic H-atoms were geometrically positioned and refined as riding. Protic H-atoms bound to heteroatoms were assigned by residual electron density. The CF_3 group is disordered over two positions and was refined using a disorder model with respective occupancies of 0.57/0.43. The structure contains voids (8.1% of unit cell volume, 109.59 Å^{3}determined with 0.3 Å grid spacing and 1.2 Å probe size). Within these voids, some residual electron density was observed but could not be modeled. Due to the kinematical refinement, the electron number definition using solvent masking algorithms led to inaccurate results and was therefore avoided, leaving the residual electron density unassigned.

Crystal Data for the 3,4-DHBA cocrystal (merged): CCDC: 2540222, $C_{26}H_{19}F_4N_7O_5$, M =585.47 g/mol, triclinic, space group *P*-1 (no. 2), a = 4.6424(4) Å, b = 17.1020(13) Å, c = 17.2070(8) Å, α = 87.353(5)°, β = 87.609(6)°, γ = 84.408(7)°, V = 1357.23(17) Å^3, Z = 2, T = 100(5) K, μ(electron) = 0.000 mm^{-1}, *Dcalc* = 1.433 g/cm^3, 26423 reflections measured (0.084° ≤ 2Θ ≤ 1.798°), 5535 unique (R_{int} = 0.1741, R_{sigma} = 0.1218) which were used in all calculations. The final R_1 was 0.1912 (I > 2σ(I)) and wR_2 was 0.4789 (all data).

Non-sink miniaturized dissolution assessment

Approx. 5 mg of solid sample were weighed into glass vials. 7 mL of FaSSIF medium (pre-warmed to 37 °C) were added and the suspension was shaken at 450 rpm at 37 °C. After 5 min, 10 min, 15 min, 30 min, 60 min, and 120 min, 1 mL suspension was withdrawn and filtered through a 0.2 μm syringe filter. Clear filtrate was analyzed by UPLC after suitable dilution to measure the amount of API dissolved, using the below UPLC method:

- Column: Acquity UPLC BEH C18 1.7μm (2.1 x 50mm)
- Solvent A: water/formic acid (999:1; v/v)
- Solvent B: acetonitrile/formic acid (999:1; v/v)
- Injection volume: 5 μL
- Column temperature: 37 °C
- UPLC -Gradient:

Time [min]	Eluent A [%]	Eluent B [%]	Flow rate [mL/min]
0	90	10	0.83
0.83	10	90	0.83
1.19	10	90	0.83
1.2	90	10	0.83

Calibration curve for determination of levels of dissolved API was established using a standard solution of free MSC178 with known concentration. UV evaluation of all chromatograms was

 doi:10.20944/preprints202603.2301.v1

performed at 343 nm. All chromatographic data analysis was performed in software Chromeleon (ver. 7.2.10).

Vehicle stability assessment of lead forms

Vehicle stability assessment was performed with 2,4-DHBA co-crystal form 24-1 and 1,2-EDSA salt form Ed-3 (samples from 50 mg upscale each). 2.5 mg of each form was weighed into a 1 mL glass vial. 500 µL of vehicle (methocel 0.5% + Tween20 0.25% in water) was added, and mixtures were treated with an Ultra Turrax device at max. speed for 1 min. Suspensions after preparation (t0) and after 24 h at room temperature storage were analyzed by Powder X-Ray Diffraction. Suspension after 24 h was investigated additionally for visual examination and pH testing (pH-Meter 780, Metrohm).

In-vivo mouse oral PK study of 2,4-DHBA co-crystal and MSC178 free base

Oral administration of the tested compounds (2,4-DHBA co-crystal form 24-1 (batch B-1) and amorphous MSC178 free base (batch A-2) were performed at an equivalent dose of 50 mg/kg of the free base in Methocel (0.5%)/Tween 20 (0.25%) in water for injection by gavage at a dose volume of 10 mL/kg in the female Crl:CD1(ICR) mice (n=3 per group, housed together in cages with elevated grid). Blood samples (20 µL) were taken sublingually 0.25, 0.5, 1, 2, 4, 6, and 24 h after oral administration using K3-EDTA-coated capillaries. Plasma was obtained by centrifugation (10,000 g; 4 °C; 5 min) and stored at - 20 ±5 °C until the bioanalytical quantification by LC-MS/MS.

The plasma concentrations were quantified by UPLC with tandem mass spectrometric detection (UPLC-MS/MS) analysis, previously developed at Nuvisan GmbH. The UPLC-MS system consisted of a Waters Acquity UPLC coupled to an AB Sciex mass spectrometer API 5500 Qtrap. The UPLC methods used a reversed-phase column (HSS T3, 1.8 µM, 2.1 x 50 mm) and elution with a short gradient starting from 0.1% formic acid in water to 0.1% formic acid in acetonitrile (see the UPLC conditions, the gradient used, and the mass spectrometer conditions in the Table below). Plasma samples (5 µL) were precipitated after addition of 20 µL internal standard solution (deuterated pruvanserine-d8) and 100 µL of acetonitrile. After centrifugation (10,000 g; 4 °C; 5 min), 50 µL of the supernatant were diluted with 100 µL water. An aliquot of 20 µL was further diluted with 180 µL acetonitrile:water (1:9, v/v) prior to analysis.

A calibration curve was prepared for MSC178 with standard samples at different concentrations using blank rat plasma.

UPLC-MS/MS method used in oral PK bioanalysis: UPLC and mass spectrometer conditions and gradient used

UPLC conditions

Column:	HSS T3, 1.8 µm, 2.1 x 50 mm
Column temperature:	60.0 ◦C
Autosampler Temperature:	10.0 ◦C
Injection Volume:	3-5 µL
Mobile Phase A:	Acetonitrile
Mobile Phase B:	0.1% Formic acid in water

Gradient

Time [min]	Eluent A [%]	Eluent B [%]	Flow rate [mL/min]
0	1	99	0.95
1.0	90	10	0.95
1.2	85	15	0.95
1.3	1	99	0.95
1.5	1	99	0.95

Mass Spectrometer Conditions

Scan Type:	MRM
Polarity:	Positive
Resolution Q1:	Unit
Resolution Q3:	Unit
Curtain Gas (CUR):	22.0 psi

 doi:10.20944/preprints202603.2301.v1

Spray Voltage:	4000 V
Source Temperature:	650 ◦C
Ion Source Gas 1(nebulizer gas):	65.0 psi
Ion Source Gas 2 (heater gas):	65.0 psi
Collision Gas (CAD):	Medium
Entrance potential (EP):	10.0 V

The maximum plasma concentration (Cmax) and time to reach the maximum plasma concentration (tmax) were obtained from the observed data. The custom-made software 'DDSTOX' developed at Nuvisan GmbH, that delivers comparable results to the validated software WinNonlin® (Princeton, New Jersey, USA), was used to calculate the area under the plasma concentration-time curve (AUC). The AUC was obtained by non-compartmental analysis with linear up/log down trapezoidal method.

5. Conclusion

Overall, the data in this study illustrate that a co-crystal strategy can be successfully developed in early pre-clinical industrial research with lean methodologies to optimize sub-optimal phys.-chem. properties of a free base. The selected 2,4-DHBA co-crystal form revealed superior properties vs an alternative co-crystal form with 3,4-DHBA as well as vs an edisylate salt form, which could be linked to intrinsic features of the crystal structure and overall particle properties of the co-crystal phase. Excellent agreement between in-vitro supersaturation behavior and in-vivo exposure gain was demonstrated for the 2,4-DHBA co-crystal form, leading to better oral absorption in vivo and lower interindividual variability in exposure compared to amorphous free base form.

Author Contributions: Conceptualization, investigation, formal analysis, visualization, writing—original draft preparation: A.B.; investigation, formal analysis, visualization, writing—original draft preparation: C.v.E.; conceptualization, writing—review and editing: L.B.; investigation, formal analysis, writing—review and editing: M.L.; writing—review and editing: D.B. All authors have read and agreed to the published version of the manuscript.

Funding: This research received no external funding.

Institutional Review Board Statement: All animal procedures were performed in accordance with the Guidelines for Care and Use of Laboratory Animals of Merck KGaA. Nuvisan GmbH has been audited by the Merck KGaA animal welfare office, and the animal work was approved by the local ethics committee. The unique study numbers were G-A-VIV-20-004 (for the 2,4-DHBA co-crystal of MSC178) and 321/19 (for the free base of MSC178). The study design and animal usage were approved by local animal welfare authorities (animal testing license ROB-55.2−2532.Vet_02−21−25, approved by the government of Upper Bavaria, Germany, Regierung Oberbayern).

Informed Consent Statement: Not applicable.

Data Availability Statement: Supporting data of reported results may be provided upon request from the authors. Cambridge Crystallographic Data Centre (CCDC) contains the supplementary crystallographic data for this publication as submitted under CCDC codes 2540221 and 2540222, respectively. This data can be obtained free of charge via www.ccdc.cam.ac.uk/data_request/cif, or by emailing data_request@ccdc.cam.ac.uk, or by contacting The Cambridge Crystallographic Data Centre, 12 Union Road, Cambridge CB2 1EZ, UK; fax: +44 1223 336033.

Acknowledgments: The following colleagues are kindly acknowledged for technical support in experimental sections: Dietrich Böse for support in providing MSC178 starting material. Michael Lange for support in g-scale upscale trials of 2,4-DHBA co-crystal form. Simone Reuter for support in in-vitro dissolution experiments. Anna Amelie Fleck for support in acquisition of Single Crystal X-Ray Diffraction structure solution of 2,4-DHBA co-crystal. Khai Nghi Truong (Rigaku Europe SE) for support in acquisition of Electron Diffraction structure

 doi:10.20944/preprints202603.2301.v1

solution of 3,4-DHBA co-crystal. Stephan Godau and Holger Kubas for support in vehicle stability study. Marcel Franke, Maximilian Scheurer and Martin Fitzner for discussions and technical support in in-silico predictions.

Conflicts of Interest: Author XXXXXXX was employed by the company XXXXXXX. The remaining authors declare that the research was conducted in the absence of any commercial or financial relationships that could be construed as a potential conflict of interest.

Abbreviations

The following abbreviations are used in this manuscript:

PK	pharmacokinetic
MSC	Merck-internal code for small-molecule compounds
POLθ	polymerase theta enzyme
COSMO / COSMO-RS	conductor-like screening model / conductor-like screening model under real solvation
2,4-DHBA	2,4-dihydroxybenzoic acid
3,4-DHBA	3,4-dihydroxybenzoic acid
1,2-EDSA	1,2-ethanedisulfonic acid
mg	Milligram
FDA	Food and Drug Administration
NCE	New chemical entity
PROTAC	Proteolysis targeting chimera
i.v.	intravenous
SEDDS	self-emulsifying drug delivery systems
ASD	amorphous solid dispersion
SDD	spray-dried dispersion
HME	hot-melt extrusion
MMEJ	microhomology-mediated end-joining
DDR	DNA damage & repair
DNA	deoxyribonucleic acid
NHEJ	non- homologous end-joining
HR	homologous recombination
FA	Fanconi anemia
pK_a	ionization constant
log P	partition coefficient octanol / water or buffer (fully un-ionized species)
log D	distribution coefficient octanol / phosphate buffer pH 7.4
HBD	hydrogen bond donor
HBA	hydrogen bond acceptor
p.o.	peroral
PEG	Polyethylene glycole
HPB	hydroxypropylbetadex
mL	Milliliter
DCS	Development classification system
PAT	process analytical technology
g	Gramm
H_{ex}	excess enthalpy
eq.	equivalents
HCl	hydrochloric acid
n.d.	not determined
IC	ion chromatography
^{1}H-NMR	proton nuclear magnetic resonance spectroscopy
°C	degree Celcius
PXRD	powder x-ray diffraction
DSC / mDSC	differential scanning calorimetry / temperature-modulated differential scanning calorimetry
C_p	heat capacity (at constant pressure)
J	Joule
K	Kelvin

 doi:10.20944/preprints202603.2301.v1

n	Number of replicates in case of multiple determinations
rh	relative humidity
BET	Brunauer-Emmett-Teller (adsorption model)
ESW	Excess Surface Work (adsorption model)
BFDH	Bravais–Friedel–Donnay–Harker (crystal morphology model)
FaSSIF	fasted-state simulated intestinal fluid
min	minutes
pH	negative decadic logarithm of molar proton concentration
ICH	International Committee for Harmonization
CLD	chord length distribution
N2	nitrogen gas
c-max	maximum observed concentration
t-max	timepoint at maximum observed concentration
AUC	area under the curve
MD	molecular dynamics
cat.-no.	catalogue number
FBRM	focused beam reflectance measurement (PAT technology)
PVM	particle view microscopy (PAT technology)
p.A.	pro analysi (analytical grade)
DPA	dew point analyser
DVS	dynamic vapor sorption
UPLC	Ultrahigh performance liquid chromatography
UV	ultraviolet

References

1. Mullard, A.; Nat Rev Drug Discov 2025, https://doi.org/10.1038/d41573-026-00001-z (accessed 02.02.2026)
2. Bhalani, D.V.; Nutan, B.; Kumar, A.; Chandel, A.S.; Bioavailability Enhancement Techniques for Poorly Aqueous Soluble Drugs and Therapeutics. Biomedicines 2022, 10(9):2055
3. Buckley, S.T.; Frank, K.J.; Fricker, G.; Brandls, M.; Biopharmaceutical classification of poorly soluble drugs with respect to "enabling formulations". European Journal of Pharmaceutical Sciences 2013, 50, 8–16
4. Syahputra, E.W.; Lee, H.; Cho, H.; Park, H.J.; Park, K.S.; Hwang, D.; PROTAC Delivery Strategies for Overcoming Physicochemical Properties and Physiological Barriers in Targeted Protein Degradation. Pharmaceutics. 2025,17, 501
5. Sharma, A.; Arora, K.; Mohapatra, H.; Sindhu, R.K.; Bulzan, M.; Cavalu, S.; Paneshar, G.; Elansary, H.O.; El-Sabrout, A.M.; Mahmoud, E.A.; Alaklabi, A.; Supersaturation-Based Drug Delivery Systems: Strategy for Bioavailability Enhancement of Poorly Water-Soluble Drugs. Molecules 2022, 27(9), 2969
6. Kendall T.; Stratford, S.; Patterson, A.R.; Lunt, R.A.; Cruickshank, D.; Bonnaud, T.; Scott, C.D.; An industrial perspective on co-crystals: screening identification and development of the less utilised solid form in drug discovery and development. Progress in Medicinal Chemistry. 2021,Vol. 60, 1st ed.
7. Burgdorf, L.; Blume, B.; Follows, B.; Lademann, C.; Dorsch, D.; Böse, D.; Finsinger, D.; Dahmen, H.; Gunera, J.; Albers, J.; Bomke, J.; Beeman, K.; Lecomte, M.; Pehl, U.; Chen, X. Discovery of MSC178, a novel orally bioavailable DNA polymerase θ inhibitor with a unique binding mode and in vivo efficacy in combination with radiotherapy and PARP inhibition. Manuscript submitted for publication.
8. Sfeir, A.; Symington, L.S. Microhomology-Mediated End Joining: A Back-up Survival Mechanism or Dedicated Pathway? Trends in Biochemical Sciences 2015, 40(11), 701–714
9. Mateos-Gomez, P.A.; Gong, F.; Nair, N.; Miller, K.M.; Lazzerini-Denchi, E.; Sfeir, A. Mammalian Polymerase θ Promotes Alternative NHEJ and Suppresses Recombination. Nature 2015, 518(7538), 254–257
10. Brambati, A.; Barry, R.B.; Sfeir, A. DNA Polymerase Theta (Polθ) – an Error-Prone Polymerase Necessary for Genome Stability. Current Opinion in Genetics & Development 2020, 60, 119–126
11. Lipinski C.A., Lombardo F., Dominy B.W., Feeney P.J.; Experimental and computational approaches to estimate solubility and permeability in drug discovery and development settings. Advanced Drug Delivery Reviews. 1997, 46 (1–3); 3–26
12. Butler, J.M., Dressman, J.B.; The Developability Classification System: Application of Biopharmaceutics Concepts to Formulation Development. Journal of Pharmaceutical Sciences. 2010, 99(12), 4940-4954

 doi:10.20944/preprints202603.2301.v1

13. Poce, G.; Consalvi, S.; Cocozza, M.; Fernandez-Menendez, R.; Bates, R.H.; Ortega Muro, F.; Barros Aguirre, D.; Ballell, L.; Biava, M.; Pharmaceutical salt of BM635 with improved bioavailability. European Journal of Pharmaceutical Sciences. 2017, 99, 17–23
14. Pantwalawalkar, J.; Kale, N.; Nangare, S.; Patil, S.; Pawar, S.; Jadhav, N.; Pharmaceutical cocrystals: Unlocking the potential of challenging drug candidates. Journal of Drug Delivery Science and Technology. 2025, 104, 106572
15. Singh, M.; Barua, H.; Jyothi, V.G.S.S.; Dhondale, M.R.; Nambiar, A.G.; Agrawal, A.K.; Kumar, P.; Shastri, N.R.; Kumar, D. Cocrystals by Design: A Rational Coformer Selection Approach for Tackling the API Problems. Pharmaceutics 2023, 15, 1161
16. Cavanagh, K.L.; Maheshwari, C.; Rodríguez-Hornedo, N. Understanding the Differences Between Cocrystal and Salt Aqueous Solubilities. Journal of Pharmaceutical Sciences 2018, 107(1), 113-120
17. Loschen, C.; Klamt, A. COSMOquick: A Novel Interface for Fast σ-Profile Composition and Its Application to COSMO-RS Solvent Screening Using Multiple Reference Solvents, Ind. & Eng. Chem. Res. 2012, 51, 14303.
18. Saal, C.; Becker, A.; Pharmaceutical salts: A summary on doses of salt formers from the Orange Book. European Journal of Pharmaceutical Sciences 2013, 49, 614–623
19. Seeram, N.P.; Bourquin, L.D., Nair, M.G.; Degradation Products of Cyanidin Glycosides from Tart Cherries and Their Bioactivities. J. Agric. Food Chem. 2001, 49, 4924–4929
20. Zhang, K, Zuo, Y.; GC-MS Determination of Flavonoids and Phenolic and Benzoic Acids in Human Plasma after Consumption of Cranberry Juice. J. Agric. Food Chem. 2004, 52, 222–227
21. Pietta, P.G.; Simonetti, P.; Gardana, C.; Brusamolino, A.; Morazzoni, P.; Bombardelli, E.; Catechin metabolites after intake of greentea infusions. BioFactors 1998, 8, 111–118
22. Klamt, A.; The COSMO and COSMO-RS solvation models; WIREs Comput Mol Sci 2018, 8:e1338
23. Reichardt, C.; Solvatochromic Dyes as Solvent Polarity Indicators. Chem. Rev. 1994, 94, 2319-2358
24. Arivazhagan, G; Parthipan, G.; Thenappan, T.; Solute–solvent interactions of acid–1,4-dioxane mixtures—By dielectric, FTIR, UV–vis and 13C NMR spectrometric methods. Spectrochimica Acta Part A. 2009, 74, 860–868
25. U.S. Department of Health and Human Services, Food and Drug Administration, Center for Drug Evaluation and Research (CDER): Regulatory Classification of Pharmaceutical Co-Crystals Guidance for Industry. 2018: https://www.fda.gov/regulatory-information/search-fda-guidance-documents/regulatory-classification-pharmaceutical-co-crystals (accessed 11.02.2026)
26. Burger, A., Ramberger, R. On the polymorphism of pharmaceuticals and other molecular crystals. I. Mikrochim Acta. 1979, 72, 259–271
27. Morris, K.R.; Structural Aspects of Hydrates and Solvates. In: Drugs and the Pharmaceutical Sciences Vol. 95, Polymorphism in Pharmaceutical Solids (ed. by H.G. Brittain), 1999, Marcel Dekker, Inc.
28. Adolphs, J.; Setzer, M.J. A Model to Describe Adsorption Isotherms. Journal of Colloid and Interface Science 1996, 180, 70-76
29. Williams, D. Measuring BET Surface Areas using Organic Probe Molecules. Surface Measurement Systems, DVS Application Note 18. From: https://surfacemeasurementsystems.com/wp-content/uploads/2022/07/App18-BET.pdf (accessed 28.01.2026)
30. Etter, M.C.; Encoding and Decoding Hydrogen-Bond Patterns of Organic Compounds. Acc. Chem. Res., 1990, 23, 120–126
31. Hartman, P.; Bennema, P.; The attachment energy as a habit controlling factor: I. Theoretical considerations. J. Cryst. Growth. 1980, 49 (1), 145-156
32. Macrae, C.F.; Sovago, I.; Cottrell, S. J. ; Galek, P. T. A.; McCabe, P.; Pidcock, E.; Platings, M.; Shields, G. P.; Stevens, J. S.; Towler, M.; Wood. P. A. Mercury 4.0: from visualization to analysis, design and prediction. J. Appl. Cryst. 2020, 53, 226-235
33. Dressman, J.B.; Reppas, C.; In vitro–in vivo correlations for lipophilic, poorly water-soluble drugs. European Journal of Pharmaceutical Sciences. 2000, 11 Suppl. 2, S73–S80
34. Lipinski, C.A.; Drug-like properties and the causes of poor solubility and poor permeability. Journal of Pharmacological and Toxicological Methods. 2000, 44, 235-249

 doi:10.20944/preprints202603.2301.v1

35. Serajuddin, A.T.M.; Salt formation to improve drug solubility. Advanced Drug Delivery Reviews. 2007, 59, 603–616
36. Stephenson, G.A.; Aburub, A.; Woods, T.A. Physical Stability of Salts of Weak Bases in the Solid-State. J. Pha. Sci. 2011, 100/5, 1606-1617
37. Basavoju, S.; Boström, D.; Velaga, S.P.; Pharmaceutical Cocrystal and Salts of Norfloxacin. Crystal Growth & Design. 2006, 6(12), 2699– 2708.
38. Li, Z.J.; Abramov, Y.; Bordner, J.; Leonard, J.; Medek, A.; Trask, A.V.; Solid-State Acid-Base Interactions in Complexes of Heterocyclic Bases with Dicarboxylic Acids: Crystallography, Hydrogen Bond Analysis, and 15N NMR Spectroscopy. J. Am. Chem. Soc. 2006, 128, 8199– 8210
39. Brouwers, J.; Brewster, M.E.; Augustijns, P.; Supersaturating Drug Delivery Systems: The Answer to Solubility-Limited Oral Bioavailability?. Journal of Pharmaceutical Sciences. 2009, 98(8), 2549-2572
40. Good, D.J.; Rodriguez-Hornedo, N.; Solubility Advantage of Pharmaceutical Cocrystals. Crystal Growth & Design. 2009, 9(5), 2252-2264
41. Chen, J.; Guo, M.; Fan, R., Peng, Y., Cai, T. Impact of bile salt on solution-mediated phase transformation of pharmaceutical cocrystals: The importance of coformer release kinetics. Chemical Engineering Journal 2022, 435, 134928
42. Li, H.; Wang, L.; Xie, G.; Yao, C.; Song, S.; Qu, Y.; Han, P.; Wang, H.; Sun, Y.; Wu, H.; Tao, X.; Cocrystals of Favipiravir: Improved Physicochemical Properties and Solution Stability Study. Crystal Growth & Design. 2023, 23, 8656-8669
43. Joshi, P.; Mallepogu, P.; Kaur, H.; Singh, R.; Sodhi, I.; Samal, S.K.; Jena, K.C.; Sangamwar, A.T.; Explicating the molecular level drug-polymer interactions at the interface of supersaturated solution of the model drug: Albendazole. European Journal of Pharmaceutical Sciences. 2021, 167,106014
44. Thakral, N.K.; Kelly, R.C. Salt disproportionation: A material science perspective. Int. Journ. Pharm. 2017, 520, 228-240
45. Becker, A.; API co-crystals – Trends in CMC-related aspects of pharmaceutical development beyond solubility. Drug Discovery Today. 2023, 28(5), 103527
46. Chen, D.; Huang, W.; Zhang, Q.; Zhang, Z.; Guo, Y.; Vreeman, G.; Sun, C.C.; Hawley, M.; Yang, B.S.; He, X.; Bioavailability-Enhancing Cocrystals: Screening, in Vivo Predictive Dissolution, and Supersaturation Maintenance. Crystal Growth & Design. 2022, 22(9), 5154-5167
47. Luedecker, D.; Hermsen, M.; Fitzner, M.; Virtual Co-Compound Screening Model. WO2025162847, 2025
48. Dolomanov, O. V., Bourhis, L. J., Gildea, R. J., Howard, J. A. K. & Puschmann, H. OLEX2: a complete structure solution, refinement and analysis program. J. Appl. Cryst. 2009, 42, 339-341
49. Sheldrick, G.M.; Crystal structure refinement with SHELXL. Acta Cryst. 2015, C71, 3-8
50. Ito, S.; White, F. J.; Okunishi, E.; ; Aoyama, Y.; Yamano, A.; Sato, H.; Ferrara, J. D.; Jasnowski, M.; Meyer, M. Structure determination of small molecule compounds by an electron diffractometer for 3D ED/MicroED. CrystEngComm 2021, 23, 8622–8630
51. Truong, K.N.; Ito, S.; Wojciechowski, J. M.; Göb, C.R.; Schürmann, C. J.; Yamano, A.; Del Campo, M.; Okunishi, E.; Aoyama, Y.; Mihira, T.; Hosogi, N.; Benet-Buchholz, J.; Escudero-Adán, E.C.; White, F.J.; Ferrara, J.D.; Bücker, R. Making the Most of ED Electron Diffraction: Best Practices to Handle a New Tool, Symmetry 2023, 15, 1555